buildings

MDPI

Article

Spatial Performance Optimization of High-Altitude Residential Buildings Based on the Thermal Buffer Effect: A Case Study of New-Type Vernacular Housing in Lhasa

Ximeng Ma, Zhen Mao and Huang Xuan *

School of Architecture, Southwest Jiaotong University, Chengdu 611756, China; maximeng@my.swjtu.edu.cn (X.M.)
* Correspondence: xuanh@swjtu.edu.cn

Abstract

High-altitude cold regions suffer from severe diurnal temperature fluctuations and limited energy supply, posing persistent challenges for maintaining indoor thermal comfort. This study investigates how the spatial configuration and thermal buffer effect can be optimized to improve the energy and comfort performance of new-type vernacular housing in Lhasa, China. Based on field-measured data, two representative housing prototypes—a self-built U-shaped dwelling and a government-designed resettlement house—were modeled and validated using EnergyPlus through the Rhino/Grasshopper platform. Parametric simulations and multi-objective optimization employing the NSGA-II algorithm were conducted to optimize both annual heating load and heating-season comfort percentage. Results show that optimized configurations combining south-facing sunspaces, north-facing enclosed corridors, and attic buffer cavities can reduce heating load by up to 80% compared with the baseline model without buffer spaces, and increase comfort duration by more than 50% under identical envelope and climatic conditions. The findings quantitatively reveal how spatial hierarchy and boundary buffering synergistically enhance passive solar utilization and thermal stability. This research establishes an integrated form–space–boundary optimization framework for energy-efficient housing design in extreme climates and provides a transferable reference for sustainable building strategies in other high-altitude regions.

Keywords: climate-resilient buildings; thermal buffer effect; extreme cold climate; high-altitude regions; passive design strategies; building energy efficiency; thermal comfort; multi-objective optimization

check for updates

Academic Editor: Eusébio Z. E. Conceição

Received: 30 September 2025
Revised: 16 November 2025
Accepted: 23 November 2025
Published: 28 November 2025

Citation: Ma, X.; Mao, Z.; Xuan, H. Spatial Performance Optimization of High-Altitude Residential Buildings Based on the Thermal Buffer Effect: A Case Study of New-Type Vernacular Housing in Lhasa. *Buildings* **2025**, *15*, 4337. https://doi.org/10.3390/buildings15234337

Copyright: © 2025 by the authors. Licensee MDPI, Basel, Switzerland. This article is an open access article distributed under the terms and conditions of the Creative Commons Attribution (CC BY) license (https://creativecommons.org/licenses/by/4.0/).

1. Introduction

As a representative high-altitude cold region, the Qinghai–Tibet Plateau experiences extreme temperature swings, strong solar radiation, and limited energy resources, making winter indoor comfort difficult to achieve. In Lhasa—the largest settlement on the Plateau—these challenges are intensified by restricted energy supply and transportation conditions [1]. Despite extensive government-led housing initiatives [2–5], field investigations show that the winter thermal performance of these newly built houses remains inadequate: indoor temperatures often stay below 10 °C, only about 0.8 °C higher than those of traditional dwellings [6–8], far below the 16 °C minimum recommended by ASHRAE 55 [9] and ISO 7730 [10].

The new-type vernacular housing examined in this study refers to the modern residential prototypes commonly found in Lhasa, including government-designed resettlement

housing and self-built new-type vernacular housing. These houses combine modern construction materials with traditional spatial layouts. Although they satisfy basic living needs, they continue to suffer from poor indoor thermal conditions during winter and therefore constitute the primary research object of this study.

Recent China-based studies in the Qinghai–Tibet context have primarily focused on envelope-centric retrofits, such as optimizing wall U-values and window properties. While simulation and field-based analyses have demonstrated the potential of such measures and established critical performance benchmarks [6,11,12]. Their implementation in economically disadvantaged high-altitude regions often requires substantial investment, posing a significant barrier to widespread adoption. More critically, these component-level optimizations have proven insufficient to address the persistent spatial non-uniformity of indoor temperatures—most notably the pronounced south–north asymmetry and chronic under-heating in winter, as consistently documented by field measurements [6,8]. In this context, an integrated approach that optimizes building massing, spatial hierarchy, and boundary design from the outset becomes paramount. Strategies that employ architectural elements such as sunspaces, enclosed north corridors, and attic cavities are particularly viable, as they function not only as effective thermal buffers but also as integral parts of the usable space [6,12–14]. This approach leverages spatial and formal reconfiguration rather than relying on costly material upgrades, making it both economically and practically feasible for these regions.

At the theoretical level, concepts such as the "temperature onion" and the "patch effect" articulate the underlying mechanisms of this approach, where the former organizes functional zones hierarchically to produce inward temperature gradients, while the latter introduces localized buffer cavities to moderate thermal peaks [15,16].

Research in high-altitude cold regions, including Tibet, consistently highlights the synergy between spatial design and thermal boundaries. Studies in Lhasa have quantitatively linked spatial form to environmental performance [13] and detailed the critical role of building interfaces in managing solar gain [17,18], underscoring the need for an integrated approach. This principle is echoed internationally: traditional Himalayan dwellings utilize spatial hierarchy and buffer zones for climate regulation [19], while Andean studies quantify the energy benefits of attached sunspaces and strategic room layouts [20]. Contemporary optimization research further confirms that coupling building morphology with envelope design is key to significant energy savings in severe cold climates. Studies conducted even in cool climate zones with high heating demands have demonstrated that optimizing a suite of envelope parameters—including window-to-wall ratio, glazing type, and wall construction—can achieve dramatic reductions in heating energy consumption [21]. Building on these foundational insights, recent optimization frameworks in Qinghai and Southern Tibet successfully integrate passive solar strategies and envelope improvements to enhance both comfort and energy efficiency [22,23], collectively validating the form–space–boundary framework advanced in this study.

Nevertheless, critical questions remain unresolved. The coupling between spatial hierarchy—the organization of direct-gain, transition, and loss-buffer zones—and boundary-buffer parameters such as sunspace depth and glazing ratio, north-corridor width, and attic-cavity height has not been quantitatively explained in terms of heating load and heating-season comfort. Most prior research optimizes individual components in isolation and does not treat form, space, and boundary conditions as an integrated system within a design-oriented, parameterized framework.

To address these gaps, this study focuses on new-type vernacular housing in Lhasa and explores three scientific questions: (1) How does spatial hierarchy affect heating-load distribution and thermal comfort under baseline conditions? (2) How do boundary-space param-

eters jointly influence building energy use and comfort? (3) Which parameter combinations yield Pareto-optimal trade-offs between heating-load reduction and comfort improvement?

Methodologically, a parameterized simulation model was developed on a Lhasa-validated baseline, representing the construction and operation conditions defined by field data and studies. Hourly simulations using EnergyPlus 9.4.0 were combined with NSGA-II bi-objective optimization (minimizing heating load and maximizing heating-season comfort duration). Through coupled analysis of form–space–boundary variables, the research extracts design thresholds and ranges. The contribution of this study lies in translating the widely recognized yet fragmented thermal buffer concept into designable, quantifiable, and tradable design ideas and methods. Furthermore, the unified baseline—based on typical construction and operation parameters for Lhasa dwellings—ensures the comparability and transferability of different optimization strategies, providing methodological and empirical guidance for designing low-energy, high-comfort residential buildings across high-altitude cold regions.

2. Methodology

2.1. Case Study and Climate Data

Lhasa is located on the Qinghai–Tibet Plateau in China at an altitude of approximately 3650 m. According to the Code for Thermal Design of Civil Buildings (GB 50176-2016) [24], it falls within the Cold Zone (A). The region is characterized by low winter temperatures, large diurnal fluctuations, and limited energy supply, resulting in persistent challenges for both building energy efficiency and indoor thermal comfort [13]. Since 2000, policies such as the "Comfortable Housing Project" and the "Relocation and Resettlement Program" during the 12th and 13th Five-Year Plans have promoted the large-scale construction of "new-type vernacular housing" in Lhasa and its surrounding areas, primarily using modern materials like concrete blocks and mortar [5,25,26].

The indoor thermal environment of new-type vernacular housing still exhibits significant seasonal fluctuations. Measurements indicate that while the daytime indoor temperature of south-facing rooms may reach 10–15 °C, rooms on the north side often remain below 10 °C, occasionally approaching 0 °C [12,27]. While these temperatures represent a marked improvement over traditional dwellings (by about 0.8 °C) [5], a direct comparison with the 16 °C threshold often cited from ASHRAE 55 and ISO 7730 requires caution. These international standards are based on the PMV–PPD model for fully heated, mechanically conditioned environments and assume standard winter clothing (≈1.0 clo) under temperate climates.

However, residential buildings in Lhasa are characterized by intermittent or partial heating, strong solar radiation, and pronounced behavioral adaptation (e.g., heavy local clothing such as Tibetan robes). Consequently, the conventional PMV framework tends to overestimate thermal discomfort in such high-altitude contexts.

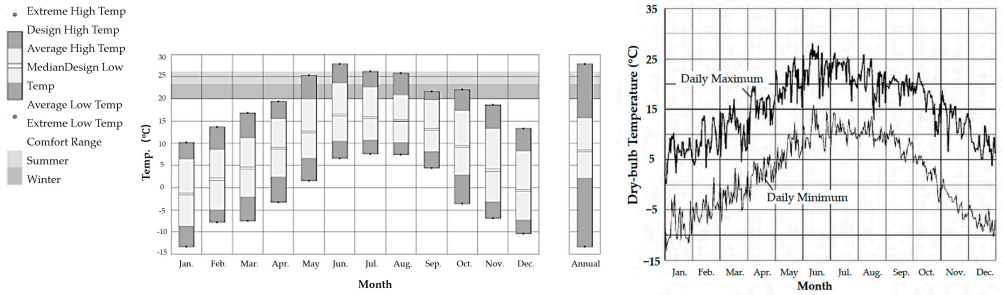
Accordingly, the APMV comfort model (GB 50736-2012) [28] was adopted to account for regional and behavioral adaptation. This provides a more realistic and regionally appropriate comfort evaluation for passively heated dwellings in Lhasa.

To support the simulation and optimization analyses, two representative prototypes of new-type vernacular housing in Lhasa were established based on on-site surveys and prior research. These prototypes capture the two prevailing construction patterns in the region: (1) Self-built dwellings, usually developed by individual households, feature flexible U- or L-shaped plans with semi-open courtyards and a depth-to-width ratio of about 1:2. Buildings are generally one to two stories high, constructed with local stone or solid bricks, and plastered with cement mortar. Their layouts prioritize solar exposure for the south-facing rooms while keeping the north side enclosed for thermal protection.

(2) Government-designed resettlement housing adopts standardized three-bedroom layouts organized in row or semi-detached forms, with concrete block walls and composite insulation systems. These houses have more uniform spatial functions and relatively compact thermal envelopes compared with self-built dwellings.

Geometric models for both types were reconstructed in Rhino7/Grasshopper according to field-measured dimensions and survey drawings, ensuring consistency with the physical prototypes described in previous studies [26,29,30].

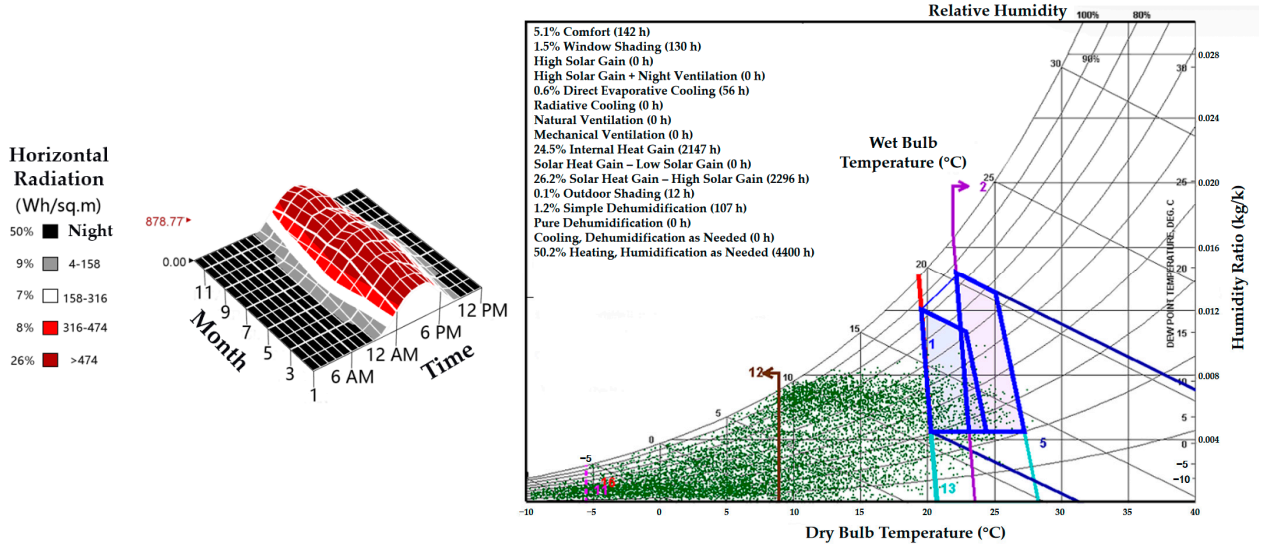
Climatic data were obtained from the Chinese Standard Weather Data for Architectural Environment Analysis (CSWD), Lhasa station (Typical Meteorological Year, TMY), providing 8760 hourly records for the simulation year. In Lhasa, China, the mean annual temperature is about 8.3 °C, with the coldest month (January) averaging −1.48 °C and the hottest month (June) with an average temperature of 16.41 °C. The annual diurnal temperature range is about 14–16 °C. Figure 1a shows the monthly temperature range and comfort band. Figure 1b shows the daily maximum and minimum temperature curves in Lhasa. Approximately 17% of the year experiences temperatures below 0 °C, 76% between 0 and 20 °C, and less than 7% above 20 °C.



(**a**) (**b**)

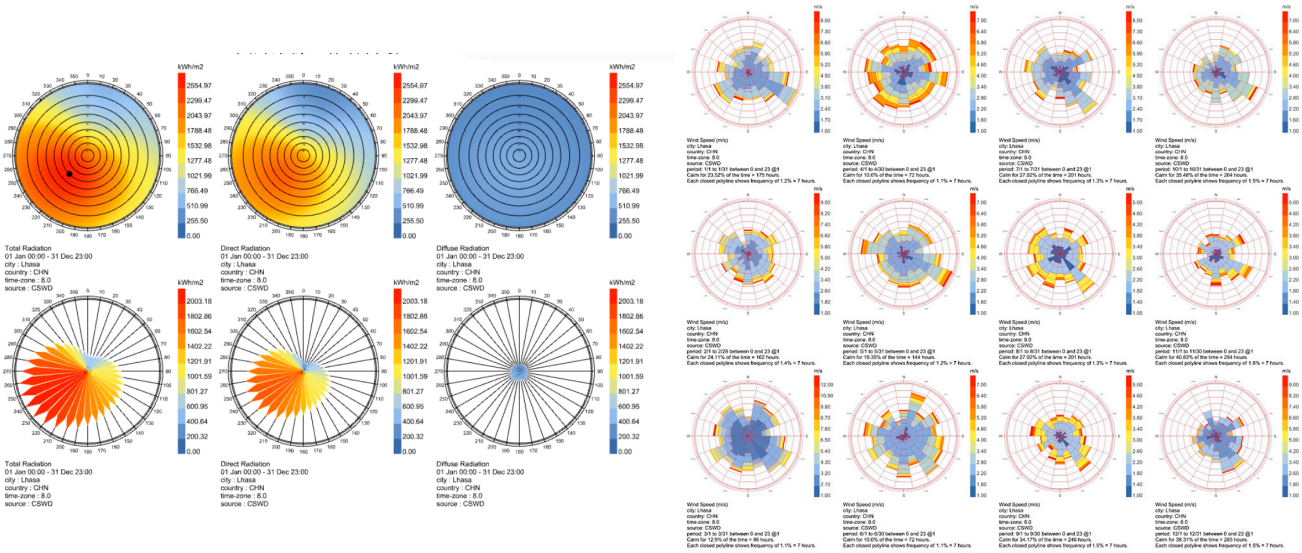
Figure 1. Temperature Patterns and Ranges in Lhasa: (**a**) Monthly Temperature and Comfort Range; (**b**) Daily Maximum and Minimum Temperature Curves in Lhasa.

Lhasa also receives strong solar radiation, with an annual horizontal radiation of about 878.77 Wh/m^2·a. Figure 2a shows the distribution of global horizontal radiation, indicating that 26% of the hourly values exceed 474 Wh/m^2. Figure 3a shows the sky matrix and radiation rose, while Figure 3b illustrates the annual wind rose for Lhasa. Analysis of the psychrometric chart and passive strategy potential (Figure 2b) indicates that heating is required for approximately 67.5% of the year. Among all passive strategies, solar gain combined with high thermal mass is by far the most applicable (effective for 26.2% of the year), whereas the potential for natural ventilation, evaporative cooling, and other strategies is very limited (each <2% annually). This analysis confirms that the climate demands a heating-dominant design approach centered on maximizing and retaining solar heat gain.



(**a**) (**b**)

Figure 2. Solar radiation and passive strategy potential in Lhasa: (**a**) Global horizontal radiation; (**b**) Psychrometric chart with passive strategy applicability.



(**a**) (**b**)

Figure 3. Lhasa Climate Analysis Chart: (**a**) Sky Matrix and Radiation Rose; (**b**) Annual Wind Rose of Lhasa.

2.2. Thermal-Buffer Framework: Thermal Buffer Strategies

The thermal buffer effect, operationalized through the "temperature onion" and "patch effect" strategies, forms the theoretical foundation of this study [31,32]. The "temperature onion" strategy, pioneered by German ecologist Thomas Herzog, involves organizing functional spaces in concentric layers based on their thermal requirements, placing the most frequently used spaces at the warm core and buffer spaces towards the exterior, thereby creating a stable, graded indoor climate [16]. In contrast, the "patch effect" strategy strengthens the building's thermal envelope by adding buffer cavities (e.g., sunspaces, double-skin walls) at its most vulnerable parts, functioning like a "patch" to mitigate localized heat loss or gain [33]. These two mechanisms address energy conservation at the spatial hierarchy and the additional boundary levels, respectively, and together form the theoretical foundation for the dual-path optimization framework proposed in this study.

2.2.1. Spatial Hierarchy

Spatial relationships involve primary and secondary distinctions in scale, form, and position. Appropriate composition can create temperature gradients and buffer effects. Common hierarchy types include core-type, internal corridor-type, external corridor-type, north–south type, perimeter-type, and vertical-type [34,35]. Among residential buildings in China, the north–south layout is particularly common. This layout places auxiliary spaces on the north side and main functional spaces on the south side, realizing a thermal strategy of "open south, closed north". Further research indicates that spatial hierarchy should be delineated according to the differentiated thermal demands of functional zones, avoiding the treatment of the interior as a homogeneous thermal field. This approach effectively enhances the utilization efficiency of solar heating [35,36].

2.2.2. Additional Boundaries

These spaces not only improve insulation performance but also enable "pre-heating and pre-cooling" regulation using natural energy sources, effectively constructing a natural heat exchange interface [33]. Typical types include: 1. Sunspace: Its forms can be categorized as projecting, recessed, and semi-projecting, with different forms significantly impacting thermal comfort [37]. The window-to-wall ratio and depth are key parameters. Excessive depth increases heating energy consumption, while a high window-to-wall ratio enhances heat gain capacity. The facade and glazing material play a crucial role in diurnal temperature fluctuations, with Low-E glass providing better insulation at night [38,39]. 2. Double-Skin Wall: Its orientation and cavity width determine insulation and thermal storage performance. Proper design can improve winter temperature levels [33].

Traditional energy-saving design often relies on thickening the building envelope in later stages, which frequently leads to diminishing marginal returns and a disjointed design process. In contrast, front-loading performance optimization to the schematic design phase shows greater potential. This study proposes an integrated approach of "Building Massing—Spatial Hierarchy—Integrated Thermal Buffer Interface." This approach entails coordinating building orientation, functional space grading, and the configuration of additional boundaries from the initial design stages. The goal is to maximize passive energy-saving potential while maintaining construction feasibility.

2.3. Baseline Definition and Assumptions

The baseline model served as the reference framework for all subsequent simulations and optimization analyses. It was established under the typical climatic conditions of Lhasa, integrating the structural characteristics and operational parameters of both self-built new-type vernacular housing and government-designed resettlement housing, as described in Sections 2.1–2.5.

All physical and operational settings follow the Thermal Design Code for Civil Buildings (GB 50176-2016) [24] and validated literature sources [6,12,16,40,41]. The baseline model assumes that the building envelope and thermal properties correspond to the locally prevalent constructions: stone–masonry walls and reinforced-concrete roofs for self-built dwellings, and composite insulated walls with hollow concrete blocks for government-designed units.

Envelope thermal parameters (wall and roof U-values, window SHGC and WWR) are summarized in Section 2.5. Climatic data inputs followed the CSWD (Lhasa station) dataset introduced in Section 2.1. Operational assumptions were standardized to ensure comparability across all experimental scenarios: mechanical cooling and natural ventilation were disabled; infiltration and ventilation rates were set to 0.3 h^{-1} and 0.5 h^{-1}, respectively; internal heat gains from occupants, lighting, and equipment were set to zero. This key sim-

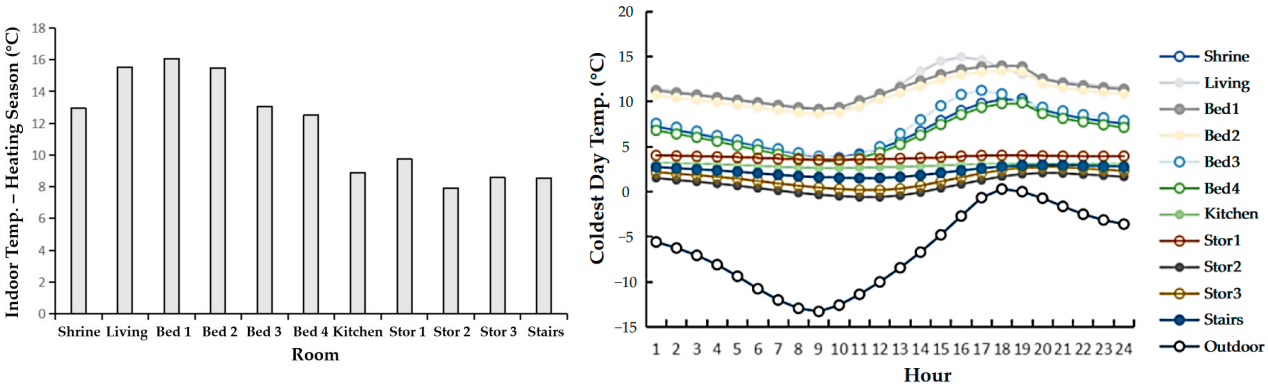
plification was adopted to iolate the intrinsic buffering effects of the form–space–boundary system and to improve computational efficiency for the optimization process. While this assumption likely leads to an overestimation of absolute heating loads, it does not alter the relative performance ranking of design alternatives, which is the primary focus of this comparative and optimization study. The heating season was defined as 15 November to 15 March, corresponding to local winter conditions. Heating setpoints were determined by functional zoning (18 °C for primary spaces, 15 °C for secondary, and 14 °C for auxiliary zones) outlined in the Residential Building Code (GB 55038-2025) [42]. The key boundary conditions for the baseline model are summarized in Table 1.

Table 1. Boundary conditions for baseline and comparative simulations.

Item	Setting
Weather and timestep	CSWD (TMY), Lhasa station (29.67° N latitude and 91.13° E longitude); hourly
Simulation periods	Heating season: Nov 15–Mar 15; Coldest day: Jan 3
HVAC	Pattern identification: heating OFF; Optimization stage: heating ON per setpoints
Cooling	OFF
Infiltration/Ventilation	0.3 h^{-1}/0.5 h^{-1}
Internal gains	0 (occupants, lighting, equipment)
Heating setpoints	18 °C (primary), 15 °C (secondary), 14 °C (auxiliary)
Constructions	Self-built: stone–masonry walls, reinforced-concrete roofs. Government-designed: composite insulated walls with hollow concrete blocks. (Detailed assemblies and U-values are provided in Section 2.5.)
Window-to-wall ratios	South: 0.45–0.50; North: $\leq$ 0.10; East/West: 0.00–0.05. (Specific values by prototype are detailed in Section 2.5.)
External obstructions	Not modeled (open-sky condition)
Solar model	Ladybug–EnergyPlus coupling using CSWD solar and radiation data
Comfort model and criterion	APMV per GB 50736-2012; Class II ($-1 \leq$ APMV ≤ 1)
Outputs	Heating load (kWh/a, kWh/m^2·a); thermal comfort (HSP); temperature and surface flux data

This gradation is consistent with the adaptive comfort standard (GB 50736-2012) [28] (Class II: $-1 \leq$ APMV ≤ 1) and reflects the differentiated thermal demands observed in field studies. Field investigations in Lhasa have shown that residents maintain thermal comfort through behavioral adaptation—such as clothing adjustment (e.g., layered garments including Tibetan robes), activity scheduling, and selective use of south-facing rooms—despite relatively low indoor air temperatures [6,18,22,41]. Core living areas typically range between 15 °C and 18 °C, while peripheral or auxiliary zones remain around 14 °C. This empirical evidence supports the adaptive zoning strategy and validates the chosen temperature gradation for high-altitude dwellings.

The baseline model was validated against published field measurements [6,13]. The simulated indoor temperature distribution successfully reproduced the characteristic winter performance, including the typical ~5 °C south–north difference. Quantitative comparison showed simulated mean temperatures of 14.3 °C (south) and 8.7 °C (north) during the heating season, consistent with the measured range of 8–16 °C [6,13]. The deviation was within ±5%, aligning with the accepted accuracy for EnergyPlus-based studies [18,23]. Figure 4 illustrates the simulated indoor temperature distribution for the representative baseline case of self-built new-type vernacular housing in Lhasa.



(**a**) (**b**)

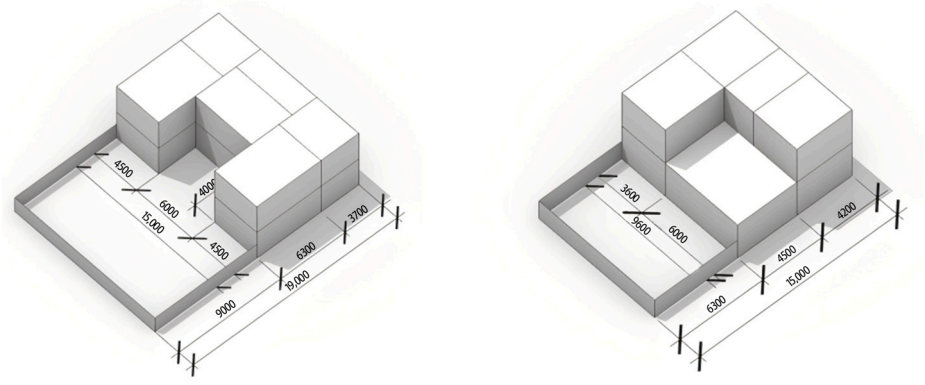
Figure 4. Simulation of Self-Built New-Type Vernacular Housing: (**a**) Heating-Season Indoor Temperature; (**b**) Coldest-Day Temperature.

The proposed baseline and workflow are transferable in principle to other high-altitude regions; however, parameter calibration (e.g., weather files, comfort criteria, envelope targets) should be localized to the climatic and regulatory context.

2.4. Model Development and Spatial Zoning

2.4.1. Geometric Modeling and Prototype Selection

This study developed two representative prototype models of new-type vernacular housing in Lhasa using the Rhino7/Grasshopper platform: ① U-shaped self-built housing (site area approx. 300 m^2, main building area approx. 150 m^2, building height 3 m, featuring a front courtyard with an activity corridor). See Figure 5a. ② Government-designed resettlement housing (typical three-bedroom layout, 150 m^2, site area approx. 150–200 m^2, main building occupies about half, in a semi-detached layout). See Figure 5b.



(**a**) (**b**)

Figure 5. Physical models of the studied residential buildings: (**a**) Self-Built New-Type Vernacular Housing; (**b**) Government-Designed Resettlement Housing.

Geometry was created in Rhino7 based on field measurements and the literature data. Using Grasshopper's geometry selection and classification functions, each space was assigned to an independent layer, ensuring traceability of spatial functional information in subsequent simulations.

The two prototypes represent the prevailing construction patterns observed in recent housing programs around Lhasa: (1) self-built courtyard-type dwellings (U-/L-shaped plans with semi-open front yards) and (2) standardized government-designed resettlement

units. Plans, dimensions, and construction assemblies were compiled from on-site surveys and published sources spanning 2012–2025, ensuring traceability of geometry and materials.

2.4.2. Spatial Zoning and Functional Grading

To reflect the differentiated thermal demands of different functional spaces in winter, this study adopted a performance-oriented zoning method during modeling, incorporating existing research on thermal comfort grading for residential buildings in the Lhasa area. Literature indicates that the comfortable temperature range for indoor spaces follows a decreasing gradient from the core to the periphery. Accordingly, this study classified indoor spaces into three tiers for the experimental setup: ① Primary functional spaces (e.g., bedroom, living room, bathroom), with a heating setpoint of 18 °C. ② Secondary functional spaces (e.g., dining room, study, scripture hall), with a heating setpoint of 15 °C. ③ Auxiliary functional spaces (e.g., staircase, corridor), with a heating setpoint of 14 °C.

2.4.3. Thermal Buffer Boundary Space Modeling

In addition to the base models, this study incorporated three key types of thermal buffer boundary spaces: ① A south-facing attached sunspace, with its depth, window-to-wall ratio, glazing construction, and roof slope set as primary parametric variables to enhance solar heat gain; ② A north-facing enclosed corridor, serving as a heat loss buffer layer, with variations in its depth included in the study; ③ A roof attic space, acting as a top insulation layer, with the cavity height reserved as a variable for subsequent optimization. The parametric setup of these boundary spaces enables flexible model adjustment and optimization.

2.4.4. Model Validation and Experimental Design

The reliability of the simulation models under the unified baseline was confirmed in Section 2.3, with the literature-based validation reproducing the characteristic south–north temperature gradient (~5 °C) for Lhasa's new-type vernacular housing [6,13]. Based on these validated prototypes, a series of comparative experiments was designed to systematically evaluate the energy-saving potential of spatial hierarchy and additional boundaries.

The variable design primarily covers three categories: building massing, spatial layout, and additional boundaries. The value ranges for various parameters were determined considering construction feasibility, local usage habits, theoretical analysis, and previous research findings.

To define the experimental scope, a range of building massing and spatial layout variables was considered, as summarized in Table 2. Among these, the building orientation and ancillary room location were pre-optimized based on findings from prior research [43], which confirmed that a 5° east-of-south orientation with centrally or north-located ancillary rooms yielded superior performance. These two parameters were therefore fixed in subsequent analyses, while the other variables listed in Table 2 were incorporated into the parametric simulation and optimization process.

Table 2. Building Massing and Spatial Layout Variables.

Category	Variable	Value/Range Description	Purpose/Significance
Horizontal Layout	Room Depth-to-Width Ratio	Typical Range: Depth 4–8 m, Width 3–6 m	To analyze the influence of horizontal dimensions on temperature distribution.
Vertical Layout	Number of Functional Floors	One Story, Two Stories, Three Stories	To verify the thermal environmental advantages of intermediate floors.
Functional Zoning	Space Tier	Primary, Secondary, Auxiliary	To hierarchically adapt to differentiated thermal comfort requirements.

At the spatial layout level, the focus was on the scale effects in both horizontal and vertical dimensions. For the horizontal layout, the impact of different spatial combinations on temperature distribution and energy consumption was analyzed by adjusting the depth-to-width ratio of main functional rooms. For the vertical layout, temperature differences between one-story, two-story, and three-story configurations were compared to verify the "intermediate floor advantage" phenomenon. Furthermore, to reveal the relationship between functional zoning and thermal environment adaptation, this study incorporated a graded division of functional spaces in the simulations. This involved combining primary, secondary, and auxiliary spaces according to differentiated thermal demands and comparing the thermal comfort performance under different matching methods.

At the additional boundaries level, this study incorporated three types of buffer spaces: sunspace, north-facing enclosed corridor, and roof attic, conducting sensitivity analysis on their key parameters. The variables and value ranges are shown in Table 3.

Table 3. Additional Boundary Variables.

Category	Variable	Value/Range Description	Purpose/Significance
Sunspace	Form	Projecting, Recessed, Semi-projecting	To compare daylighting and heat gain effects of different spatial forms.
	Window-to-Wall Ratio	0.4–1.0	To balance heat gain and heat loss.
	Depth	1.0–3.0 m	To control solar radiation utilization and energy consumption.
	Glazing Type	Single-pane, Double-pane Low-E	To compare differences in heat gain and insulation performance.
	Roof Slope	25–65°	To optimize heat collection efficiency in regions with low solar altitude.
	Skylight Area Ratio	0–20%	To analyze the impact of additional daylighting and heat dissipation.
North-facing Corridor	Depth	1.0–2.5 m	To evaluate the heat loss buffering effect.
Attic Space	Cavity Height	0–2.3 m	To regulate the stability of the top-floor thermal environment.
	Insulation Thickness	0–200 mm	To reduce heating load and improve overall insulation performance.

All variables were simulated using a one-factor-at-a-time sequential variation approach to clarify their sensitivity and contribution to thermal comfort and heating energy consumption. Subsequently, key parameters with significant influence were incorporated into the multi-objective optimization process, using a genetic algorithm to seek balanced solutions between energy consumption and comfort.

In addition, for the three types of additional boundary spaces (sunspace, north-facing corridor, and attic roof), a local one-at-a-time (OAT) sensitivity analysis was performed. Quantitative results are reported in Section 3.4.

(To avoid redundancy, the boundary conditions of the stratification test and the evaluation indicators and setpoints are uniformly listed in Section 2.6).

2.5. Envelope and Material Properties

To ensure the accuracy of the simulation results, the study specifies the envelope material parameters of typical new vernacular dwellings, distinguishing between self-built

houses and government-designed resettlement housing. The data are primarily derived from field investigations and relevant literature [41], and calibrated with the Design Code for Thermal Insulation of Civil Buildings (GB 50176-2016) [24].

For self-built "U-shaped" new vernacular dwellings, the external wall structure commonly adopts cement plaster + stone brick + cement plaster, with an overall U-value of approximately 1.44 W/(m^2·K). The roof is typically reinforced concrete with a leveling layer, with a U-value of 1.20 W/(m^2·K). The window-to-wall ratio (WWR) of south-facing facades is about 0.45–0.50, north-facing facades are no greater than 0.10, while east- and west-facing facades remain essentially closed. Exterior windows are single-pane glazing with aluminum alloy frames, with a U-value of 6.5 W/(m^2·K) and a solar heat gain coefficient (SHGC) of approximately 0.73.

For government-designed resettlement housing, the external wall typically adopts a composite system of cement plaster—inorganic insulation mortar—hollow concrete block—inorganic insulation mortar—cement plaster, with a U-value of about 1.08 W/(m^2·K). Roofs are combined with insulation layers, with a U-value of 0.45 W/(m^2·K). Windows are double-glazed units (6 mm + 12 mm air gap + 6 mm), with a U-value of 2.67 W/(m^2·K) and an SHGC of about 0.49 [6,12,25,29,41]. The detailed material layers, thermal properties, and window-to-wall ratios for both construction assemblies are summarized in Tables 4–8.

Table 4. Thermal Properties of Opaque Envelope Construction for New Vernacular Dwellings (Construction Assembly 1).

Envelope Component	Layer Description and Thickness	Thickness (m)	Thermal Conductivity (W/(m·K))	Density (kg/m^3)	Specific Heat Capacity (J/(kg·K))
External Wall	Cement plaster	0.020	0.930	1800	1050
	Stone brick	0.580	1.160	2000	920
	Cement plaster	0.020	0.930	1800	1050
Internal Wall	Stone brick	0.560	1.160	2000	920
	Cement plaster	0.020	0.930	1800	1050
Roof	Cement plaster	0.020	0.930	1800	1050
	Reinforced concrete	0.120	1.740	2500	920
	Cement plaster	0.020	0.930	1800	1050
	Roofing felt	0.003	0.170	600	1470
Floor Slab	Cement plaster	0.020	0.930	1800	1050
	Reinforced concrete	0.120	1.740	2500	920
	Cement plaster	0.020	0.930	1800	1050

Table 5. Thermal Properties of Transparent Building Envelope for New Vernacular Dwellings (Construction Assembly 1).

Envelope Assembly	Material Description	U-Value (W/m^2·K)	Solar Heat Gain Coefficient (SHGC)
Exterior Window	Single-pane glazing with aluminum alloy frame	6.5	0.73

Table 6. Thermal Properties of Opaque Building Envelope for New Vernacular Dwellings (Construction Assembly 2).

Envelope Assembly	Material Layer	Thickness (m)	Thermal Conductivity (W/(m·K))	Density (kg/m^3)	Specific Heat Capacity (J/(kg·K))
External Wall	Cement plaster	0.020	0.930	1800	1050
	Inorganic insulation mortar	0.030	0.180	600	1050
	Concrete hollow block	0.300	0.750	1500	920
	Inorganic insulation mortar	0.030	0.180	600	1050
	Cement plaster	0.020	0.930	1800	1050
	Cement plaster	0.020	0.930	1800	1050
Internal Wall	Concrete hollow block	0.200	0.750	1500	920
	Cement plaster	0.020	0.930	1800	1050
	Cement plaster	0.050	0.930	1800	1050
Roof	XPS (Extruded Polystyrene)	0.150	0.028	32	1380
	Reinforced concrete	0.100	1.740	2500	920
	Cement plaster	0.020	0.930	1800	1050
	Cement plaster	0.020	0.930	1800	1050
Floor Slab	Reinforced concrete	0.120	1.740	2500	920
	Cement plaster	0.020	0.930	1800	1050

Table 7. Thermal Properties of Transparent Building Envelope for New Vernacular Dwellings.

Envelope Assembly	Material Description	U-Value (W/m^2·K)	Solar Heat Gain Coefficient (SHGC)
Exterior Window	Aluminum alloy frame, double-glazed window (4 mm + 12 A Argon + 4 mm, medium-transmittance glass)	2.67	0.49

Table 8. Window-to-Wall Ratio (WWR).

Orientation	South Facade	East and West Facades (Gable Walls)	North Facade
WWR	0.45–0.50	0.00–0.05	$\leq$0.10

In addition, the sensitivity analysis of wall material thermal conductivity and floor heat storage performance indicates that, within the range of commonly used materials, their impact on indoor temperature and energy consumption is significantly smaller than that of parameter variations in additional boundary spaces. Therefore, these factors are not discussed separately in the Section 3.

2.6. Simulation and Optimization Framework

Based on the established baseline model and boundary conditions defined in Section 2.3, all simulations and optimization analyses were carried out using an integrated workflow developed on the Rhino7/Grasshopper platform. The framework established a continuous link between parametric modeling, dynamic energy simulation, and multi-objective optimization, ensuring traceable data flow from design variables to performance outputs (Figures 6 and 7). This approach avoided the fragmented "model–export–reimport" process typical of conventional software workflows, allowing consistent evaluation of spatial and thermal parameters under the same boundary conditions. The specific procedures and algorithmic details of each module are illustrated in subsequent sections.

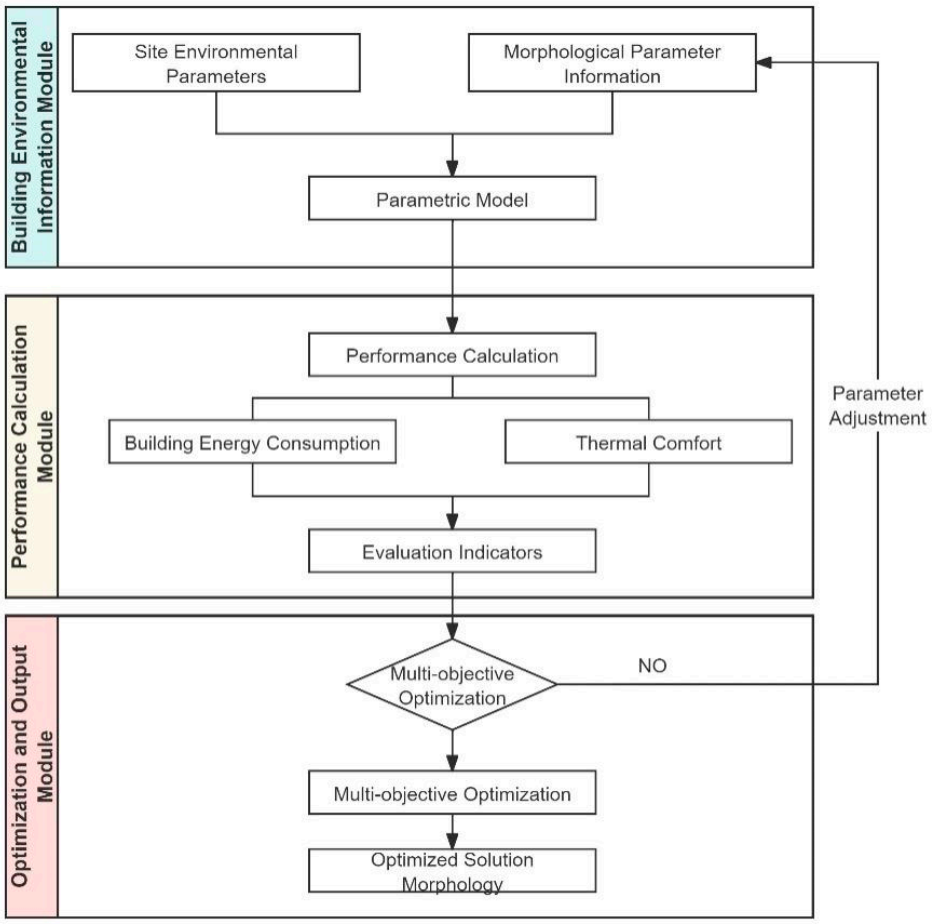


Figure 6. Integrated methodological framework linking case study, model development, simulation, and optimization processes.

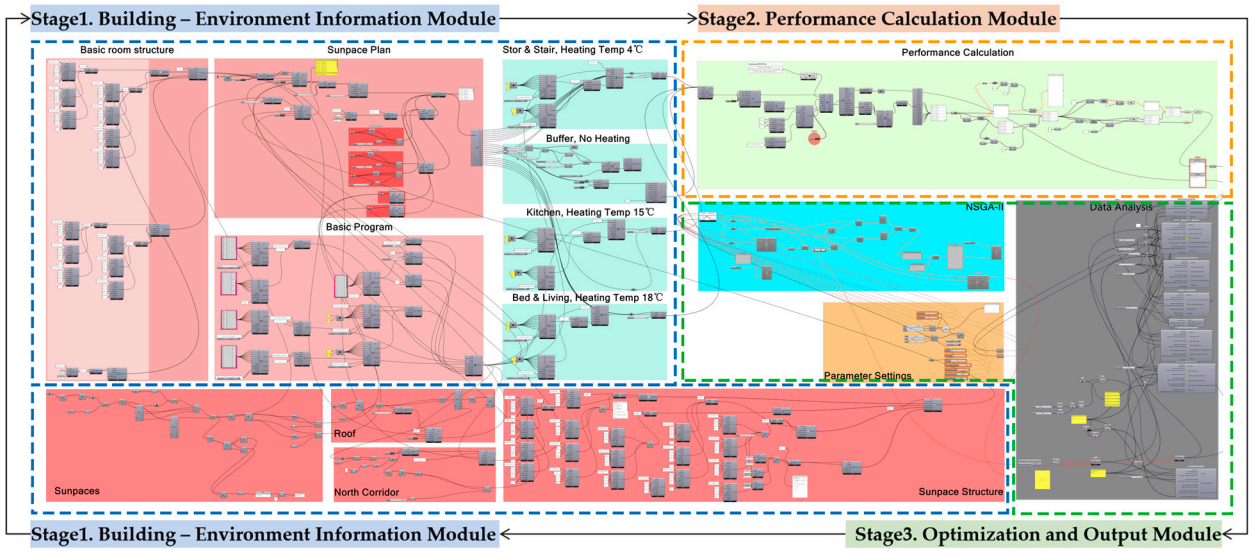


Figure 7. The integrated simulation–optimization workflow developed in Grasshopper.

(1) Building–Environment Information Module

This module provided the geometric, material, and climatic inputs required for the simulations. Weather data for the Typical Meteorological Year were imported from the CSWD Lhasa station using the EPWMap interface in Ladybug. The baseline and parametric building models were created in Rhino7 according to field-measured dimensions and

validated sources, and then imported into Grasshopper for data organization and parameter control. Each functional space was assigned to an independent layer to ensure consistency with the zoning scheme established in Section 2.4.

Thermal buffer components—including the south-facing sunspace, north-facing enclosed corridor, and attic roof—were parameterized in Grasshopper, with their depth, height, window-to-wall ratio, and insulation thickness defined as adjustable variables for later optimization. Envelope and operational attributes were linked to the ConstructionSet and Setpoint nodes, ensuring that EnergyPlus correctly interpreted thermal properties and boundary conditions; all baseline inputs followed the unified settings in Table 1.

(2) Performance Calculation Module

Dynamic thermal simulations were conducted through the Honeybee–EnergyPlus interface, using hourly timesteps and the "Full Exterior" solar radiation model. Simulations were conducted under the unified baseline conditions (Table 1).

EnergyPlus outputs—including air temperature, surface heat flux, and zone heating demand—were exported as SQL datasets and processed within Grasshopper for post-analysis. Performance metrics (annual heating load; HSP based on APMV Class II) followed the definitions and thresholds introduced earlier (Sections 2.1 and 2.3) and were post-processed in Grasshopper.

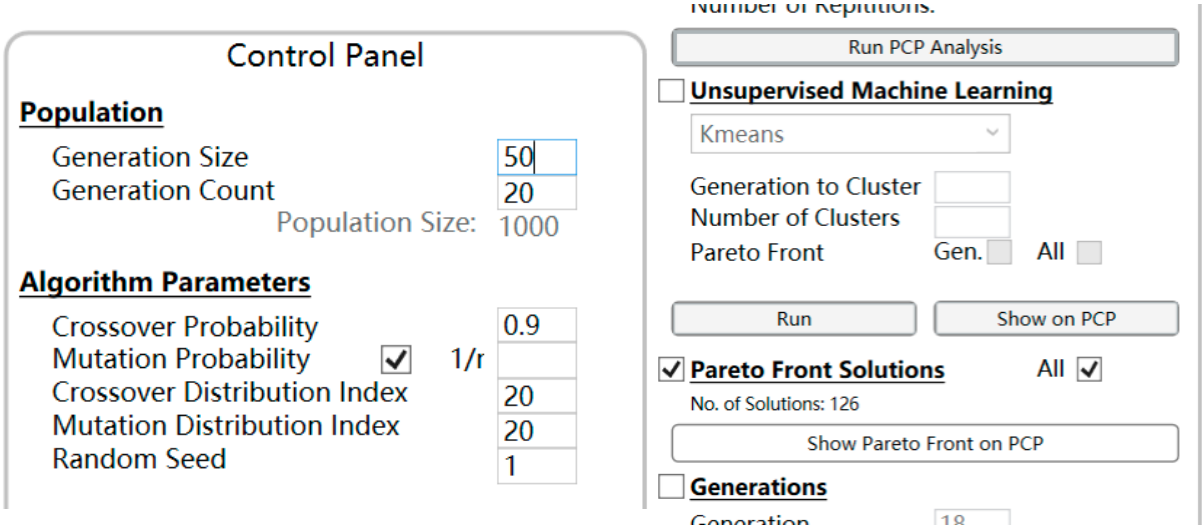
Supplementary indicators included the average indoor temperature, south–north temperature gradient, and energy-saving rate relative to the baseline model. These metrics formed the objective and evaluation functions for the subsequent optimization process.

(3) Optimization and Output Module

The optimization and output module implemented the Non-Dominated Sorting Genetic Algorithm II (NSGA-II) through the Wallacei plug-in in Grasshopper. Optimization variables were derived from the sensitivity analysis in Section 2.4.4 and categorized into three groups: (1) sunspace geometry (depth, window-to-wall ratio, glazing type, roof slope, skylight ratio); (2) north-facing corridor depth; (3) attic cavity height and insulation thickness.

The algorithm followed the standard NSGA-II structure with fast non-dominated sorting and crowding-distance elitism to preserve diversity along the Pareto front [44]. A light hyperparameter sweep (population 30–80; generations 10–40; crossover 0.80–0.95) was conducted, and the final parameters were set to a population of 50, 20 generations, a crossover rate of 0.9, and the default mutation rate (Figure 8). This configuration achieved stable convergence and balanced solution diversity, consistent with previous NSGA-II applications in building design optimization [45,46]. Each optimization run (20 generations $\times$ 50 individuals) required approximately 12 h on an Intel i7 workstation (32 GB RAM). A total of two such runs were conducted for the two prototypes, resulting in a combined 2000 solutions.

Upon completion, Wallacei generated (1) a Pareto-front solution set illustrating the trade-off between heating load and comfort (HSP) and (2) an evolutionary record for convergence analysis. The Euclidean distance method was used to identify the optimal compromise solution. Results were exported via TT Toolbox for post-analysis (Sections 3.4 and 3.5).



(**a**) (**b**)

Figure 8. Indicator parameter settings: (**a**) result extraction; (**b**) Parameter settings of the evolutionary algorithm (Grasshopper screenshot).

3. Results and Discussion

All energy and comfort indicators reported in this section follow the definitions and criteria described in Section 2.6.

3.1. Baseline Thermal Environment and Space-Type Definition

Under the unified boundary conditions described in Section 2, baseline simulations were performed for the heating season (15 November–15 March) and for the coldest day (3 January) to characterize the intrinsic winter indoor environment of the two representative dwelling prototypes in Lhasa.

Without active heating, both prototypes exhibited pronounced spatial non-uniformity: south-facing rooms maintained average air temperatures approximately 5 °C higher than north-facing rooms, and second-floor spaces were generally 1–2 °C warmer than the first and third floors, indicating a clear "middle-floor advantage." These features, along with the quantitative baseline performance (validated in Section 2.3), confirm that the model reproduces the characteristic spatial distribution patterns observed in practice [6,13].

Consistent with the zoning rationale in Section 2.4.2, two spatial types were defined for use in later analyses:

(1) **Direct Heat-Gain Spaces (DHS)**—rooms that receive substantial direct solar radiation under baseline conditions (typically south- or southwest-facing); and

(2) **Loss-Buffer Spaces (LBS)**—rooms that primarily act as thermal buffers with limited solar gains (typically north- or northeast-facing).

The DHS–LBS distinction provides the analytical framework for evaluating how design parameters influence winter heating demand and the Heating-Season Comfort Percentage (HSP) in the following sections. Figure 4 illustrates representative spatial temperature fields for the heating season and the coldest day.

3.2. Scale Effects and Functional-Grading Response

Consistent with the pre-optimized parameters defined in Section 2.4.4, a 5° east-of-south orientation with centrally or north-located ancillary spaces was adopted for all models.

After establishing the fixed boundary settings, this section further examines how variations in horizontal and vertical spatial scales influence the indoor thermal environment

of the two dwelling models constructed with the envelope parameters defined in Section 2.5 (Construction Assembly 1 and 2).

Controlled-variable numerical simulations were conducted under identical boundary conditions, focusing on the effects of depth and height variations in DHS and LBS, with the specific parameter ranges detailed in Table 9, the simulation model is shown in Figures 9 and 10. The analyses covered both the heating season and the coldest day, ensuring consistency with the climatic boundaries defined in Section 2. Because the spatial distribution patterns were nearly identical for both envelope assemblies, results based on Construction Assembly 1 are presented as representative in the following figures.

Table 9. Simulation parameter ranges.

Unit	Variable	Value Range	Data Type	Step Size
Direct Heat Gain Space	Depth	4.6–6.3 m	Continuous	0.3
	Width	0.0–4.5 m	Continuous	1.5
	Clear Height	2.8–3.3 m	Continuous	0.1
Heat Loss Buffer Space	Depth	3.6–4.5 m	Continuous	0.3
	Clear Height	2.8–3.3 m	Continuous	0.1

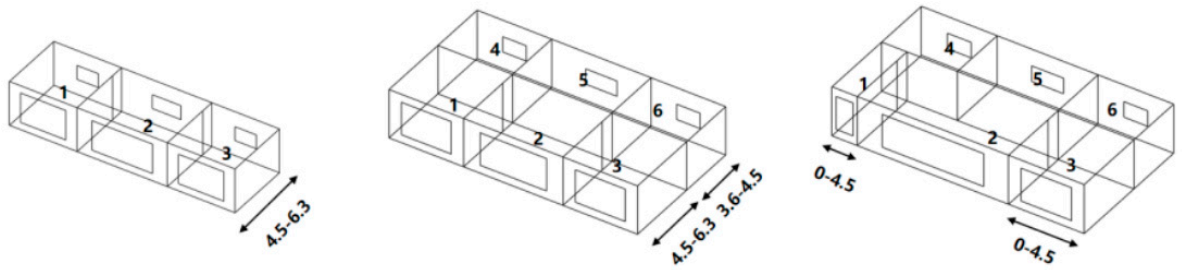


Figure 9. Horizontal simulation working conditions.

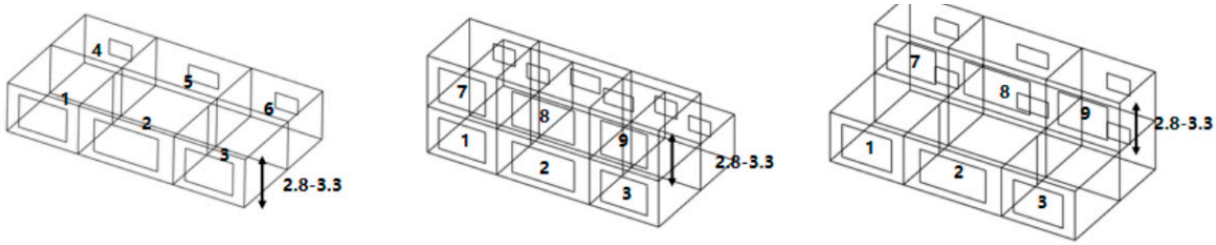
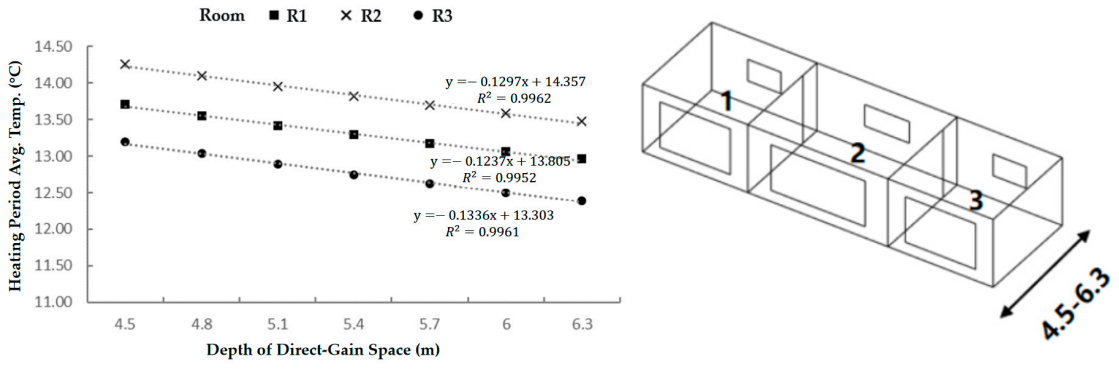


Figure 10. Vertical simulation working conditions.

3.2.1. Horizontal Scale Effects of Layout

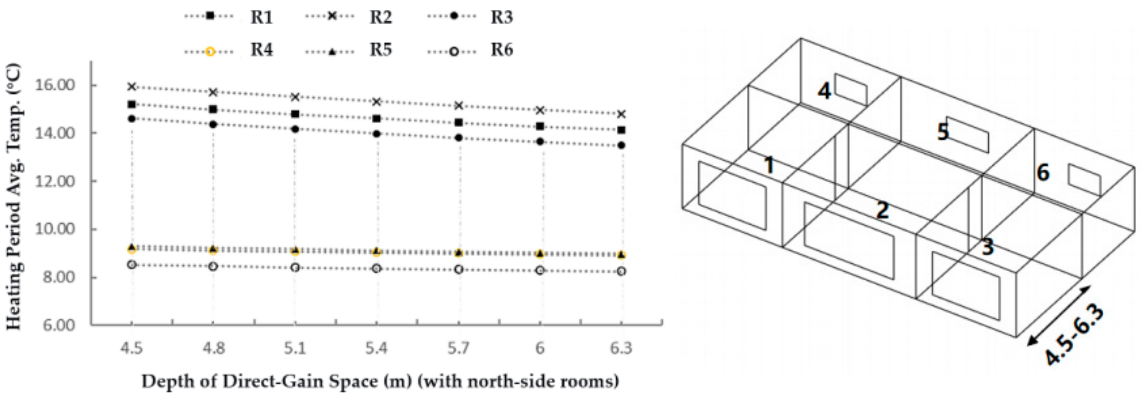
The horizontal scale effects were analyzed by varying the depths of DHS and LBS under the fixed boundary settings described in Section 2. Consistently across both Construction Assemblies, the simulations revealed clear and repeatable response patterns.

When no north-side buffer space was present, increasing the DHS depth from 4.5 m to 6.3 m led to declines in heating-season average temperatures in three representative rooms by approximately 0.75 °C, 0.78 °C, and 0.80 °C, respectively (Figure 11). With a north-side buffer added, the same increase in DHS depth caused only a −0.28 °C drop in the south-facing room and a −0.26 °C drop in the buffer zone (Figure 12). Moreover, introducing a 3.6 m north-facing buffer increased the average temperature of south-facing primary rooms by >1.5 °C (Figure 13), while further deepening from 3.6 m to 4.5 m produced negligible additional gains (<0.10 °C in south rooms; ≈0.07 °C in the buffer).



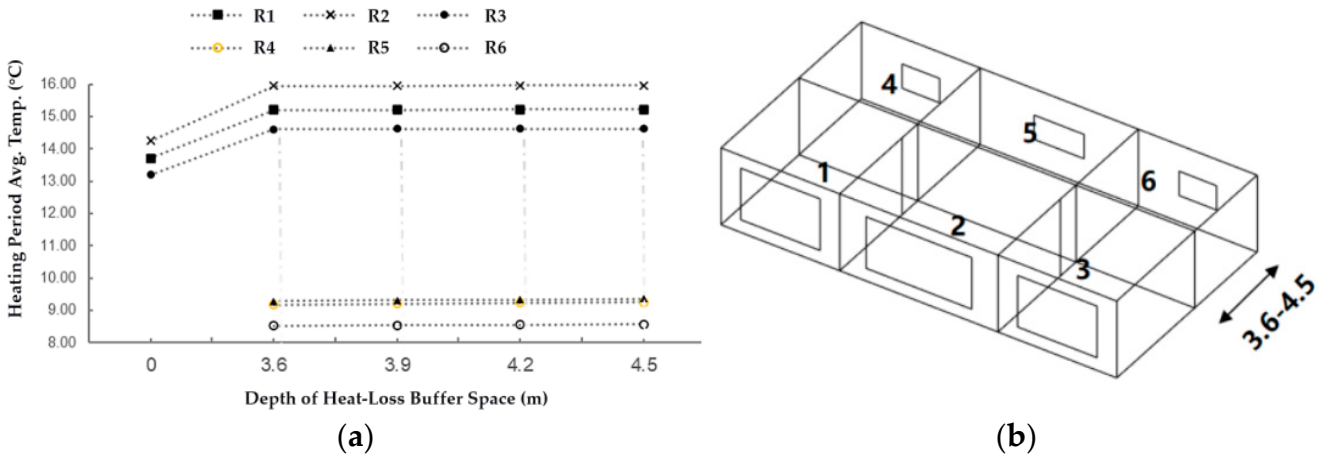
(**a**) (**b**)

Figure 11. Direct heat-gain space (without north-side room): (**a**) relationship between depth variation and indoor temperature; (**b**) simulation cases.



(**a**) (**b**)

Figure 12. Direct heat-gain space (with north-side rooms): (**a**) curve of depth variation vs. indoor temperature; (**b**) simulation cases.



(**a**) (**b**)

Figure 13. Heat-loss buffer space: (**a**) curve of depth variation vs. indoor temperature; (**b**) simulation cases.

Increasing DHS depth lengthens the solar penetration path and expands low-irradiance inner zones, which weakens net solar gains and amplifies DHS–LBS temperature gradients. A north buffer, in contrast, cuts conductive/convective losses to the exterior and moderates the gradient, so the adverse effect of larger DHS depth is partly offset. The combined behavior indicates a practical optimum: DHS depth around 5.1–5.4 m balances

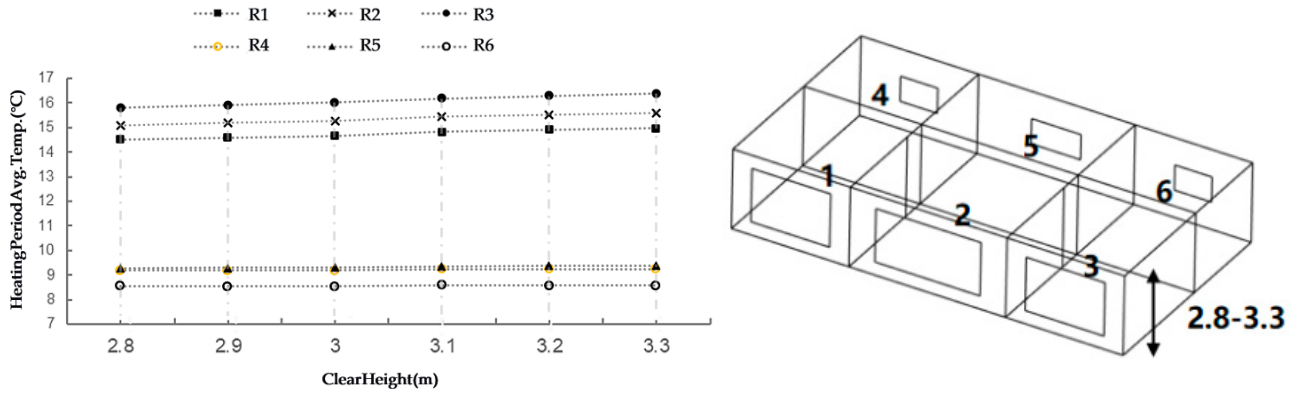
usable solar gain and thermal stability, while a ~3.6 m north buffer achieves most of the buffering benefit with diminishing returns beyond that value.

Control DHS depth at ≈5.1–5.4 m and provide a ~3.6 m north-side buffer to flatten spatial gradients and reduce heating load.

3.2.2. Vertical Scale Effects of Layout

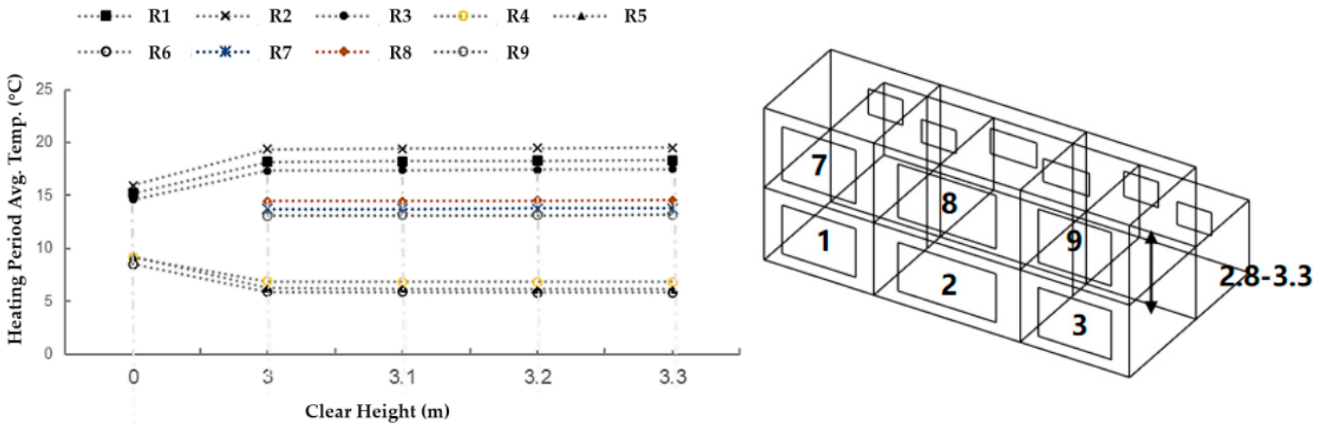
Vertical scale effects were examined through two variables under identical boundary conditions: overall clear height and the addition of partial second-floor segments at different positions.

Increasing the clear height from 2.8 m to 3.3 m slightly raised heating-season average temperatures by ≈0.3 °C across rooms (Figure 14). When a partial second floor was added above the south-side DHS, the underlying south room warmed by ≈+3.0 °C, but the north room cooled by ≈−2.6 °C due to shading (Figure 15), yielding a non-uniform building-scale impact on heating load and HSP. By contrast, placing the partial second floor above the north-side LBS increased average temperatures by ≈+1.19 °C (south) and ≈+3.33 °C (north), mitigated nighttime troughs, and more consistently reduced heating load while improving HSP (Figure 16).



(**a**) (**b**)

Figure 14. First-floor clear height: (**a**) curve of clear height variation vs. indoor temperature; (**b**) simulation cases.



(**a**) (**b**)

Figure 15. Direct heat-gain space with partial second floor: (**a**) curve of temperature variation vs. indoor temperature; (**b**) simulation cases.

A modest height increase enlarges window aperture area at a fixed WWR and improves winter solar capture; the additional volume penalty is small under the studied climate, hence the net +0.3 °C gain. For partial second floors, location dominates performance: above DHS (south), the added mass/cover enhances local gains but casts penalizing shade toward the north, worsening inter-room imbalance; above LBS (north) it works as an added thermal shield, reducing roof/sky exposure and stabilizing the whole-building temperature field.

Prefer moderate height increases (2.8 → 3.3 m) and, if a partial second floor is needed, place it above LBS (north) rather than above DHS (south) to balance insulation and solar access.

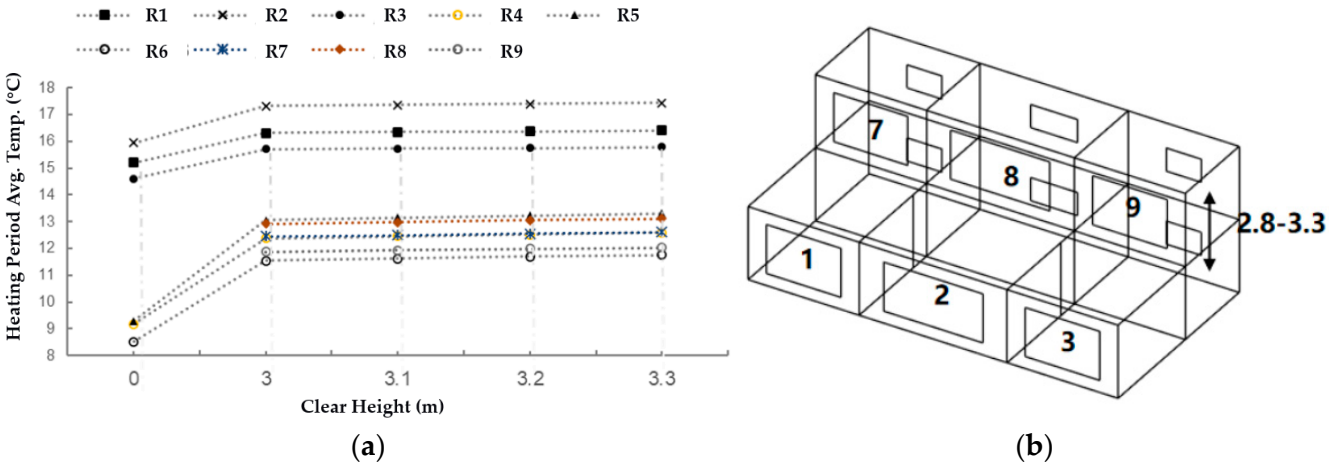


Figure 16. Heat-loss buffer space with partial second floor: (**a**) curve of temperature variation vs. indoor temperature; (**b**) simulation cases.

3.2.3. Functional Spatial Thermal Comfort Grading and Application Effects

Following the target indoor temperature settings for different functional spaces described in Section 2.4.2, the simulation results were further analyzed to establish a functional–thermal grading framework for residential layouts in Lhasa [47]. The heating design principles followed the tiered setpoints (18/15/14 °C) specified in GB 55038–2025. Based on these differentiated comfort requirements, all rooms were classified into three functional categories—primary, secondary, and auxiliary—and mapped onto the five comfort grades (I–V) summarized in Table 10.

Table 10. Classification of indoor spatial thermal comfort.

Grade	Spatial Combination and Shading/Buffer Characteristics	Typical Spatial Attributes (DHS/LBS)	Temperature Performance During Heating Period (Key Results)
I	Unshaded, south-facing DHS, with buffer spaces on east, west, and north sides	DHS (multi-sided buffer)	Highest average temperature, smallest diurnal variation
II	Unshaded DHS, with buffer spaces on two sides	DHS (double-sided buffer)	High average temperature, relatively small variation
III	Unshaded DHS, with only one-sided buffer or central space	DHS/Central	Moderate average temperature, moderate variation
IV	Obvious shading, buffer spaces on both sides	DHS/LBS (shaded)	Relatively low average temperature, relatively large variation
V	Shaded, only one-sided buffer (mostly north-facing LBS)	LBS (single-side buffer)	Lowest average temperature, significant night drop

In this framework, Grades I–II correspond to south-facing DHS with higher stability and minimal diurnal variation, Grade III represents central or semi-buffered spaces, while Grades IV–V correspond to north-facing LBS that mainly serve as heat-loss buffers with lower average temperatures.

Applying this classification to the two envelope configurations (Construction Assembly 1: self-built dwelling; Construction Assembly 2: government-designed dwelling), the DHS zones were primarily located on the south or southwest sides and fell into Grades I–II, while LBS zones appeared on the north or northeast sides, mostly Grades IV–V. These spatial patterns are shown in Figure 17, which illustrates the comfort zoning of both prototypes under baseline conditions.

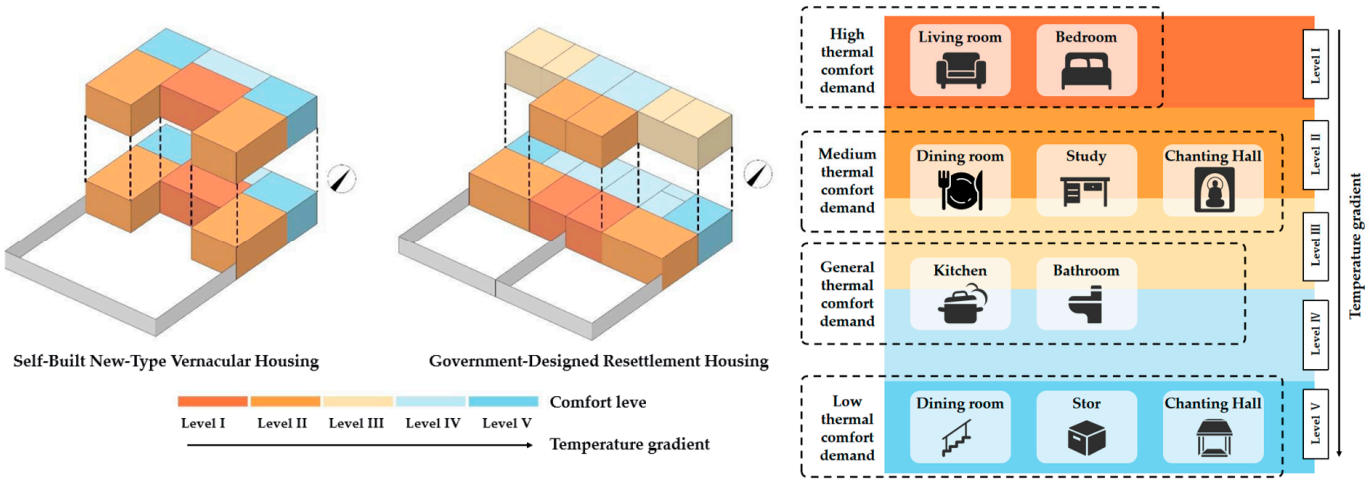


Figure 17. Spatial distribution of indoor comfort grades (Grades I–V) in Construction Assemblies 1 and 2.

To evaluate the quantitative effects of matching thermal comfort grades with functional zoning, two layout optimization scenarios were simulated under consistent envelope performance and window-to-wall ratios. The total area of primary and secondary spaces was constrained within ±1.5% of the baseline, and the overall shape coefficient remained nearly constant to isolate the impact of spatial reorganization.

In the self-built dwelling (Construction Assembly 1), auxiliary rooms such as storage and corridors were repositioned to form shallow east–west side belts about 1.5 m wide adjacent to the southern DHS, while the kitchen was relocated to the north-central zone. The primary living and sleeping rooms were deepened to approximately 7.3 m, slightly reducing their width to maintain compactness. As a result, most primary spaces were upgraded from Grade II to Grade I, and the kitchen from Grade V to Grade IV. The heating load decreased markedly from 12,465.81 kWh/a to 7611.70 kWh/a (a reduction of 38.93%), and the heating-season comfort percentage (HSP) rose from 30.95% to 35.70%—an increase of 15.35%. The baseline and optimized plans are presented in Figure 18, and the comparative thermal performance is shown in Figure 19.

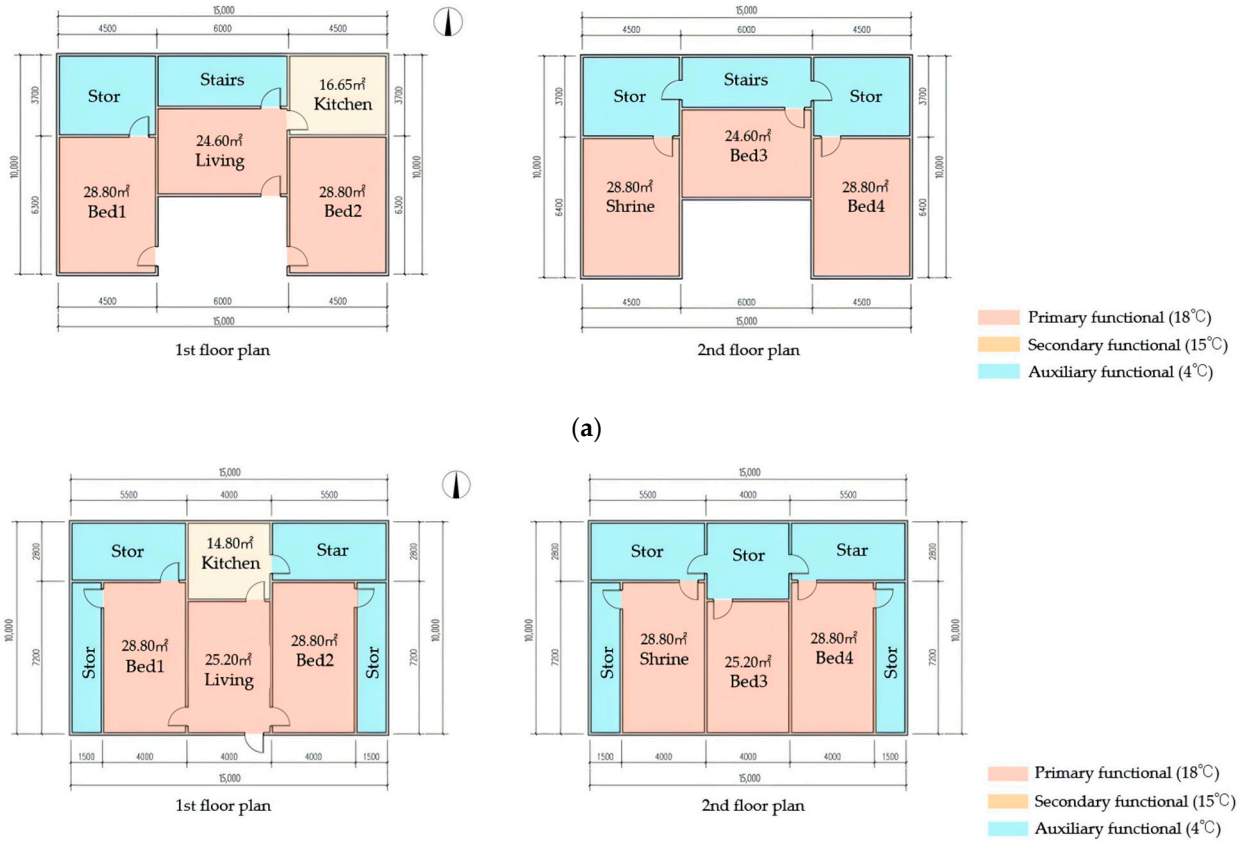


Figure 18. Layout optimization for the self-built dwelling: (**a**) baseline layout; (**b**) optimized layout.

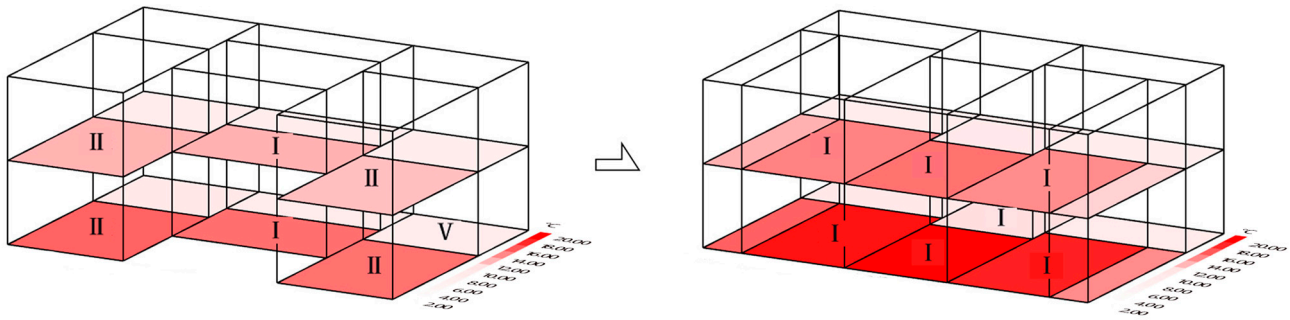


Figure 19. Distribution of indoor comfort grades before and after optimization for Construction Assembly 1.

For the government-designed dwelling (Construction Assembly 2), auxiliary functions (bathrooms, storage rooms) were placed along the east and west sides of the living room, and the living room depth was increased from 5.1 m to 5.7 m while keeping the total floor area nearly unchanged. After optimization, the living room was upgraded from Grade II to Grade I, and surrounding buffer spaces strengthened thermal wrapping on the south. The heating load decreased from 6 631.39 kWh/a to 6 152.62 kWh/a (a reduction of 7.22%), while HSP increased from 32.00% to 37.73% (an increase of 17.9%).

The optimization results are summarized in Figure 20, showing the reorganization of functional spaces, and in Figure 21, which presents the new comfort zoning pattern.

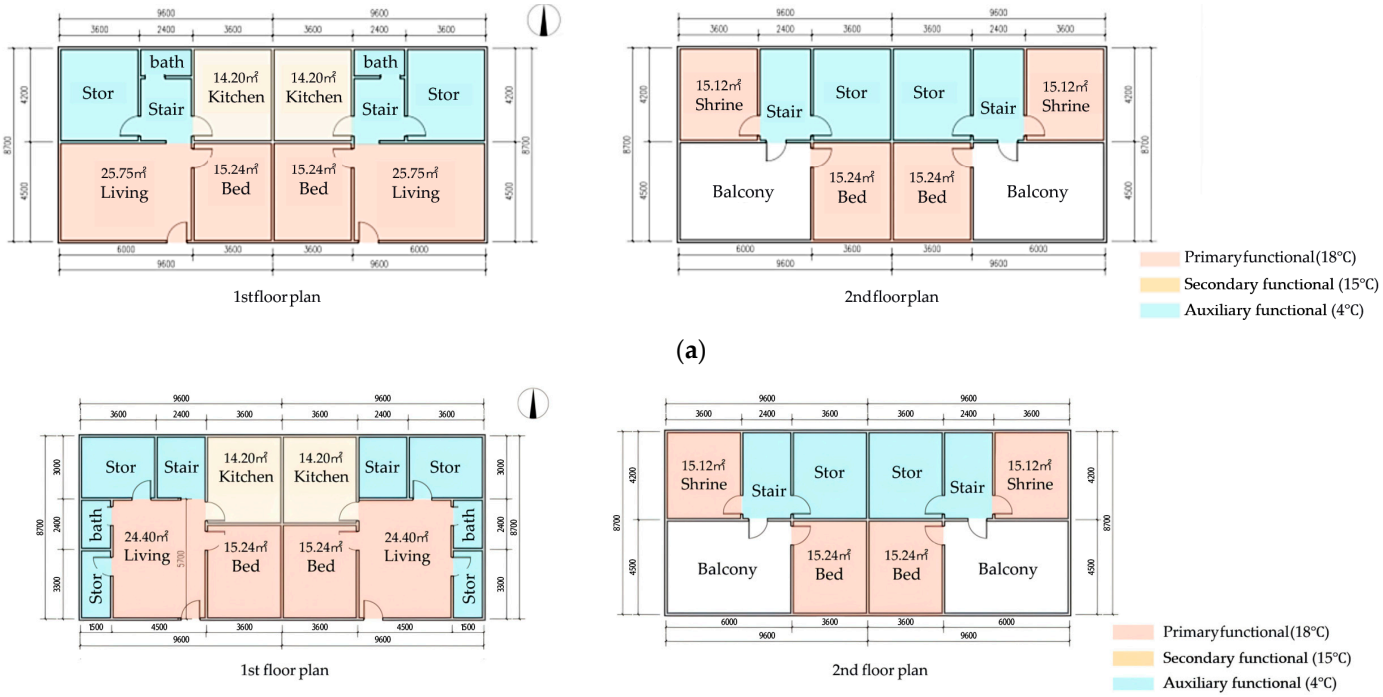


Figure 20. Layout optimization for the government-designed dwelling: (**a**) baseline layout; (**b**) optimized layout.

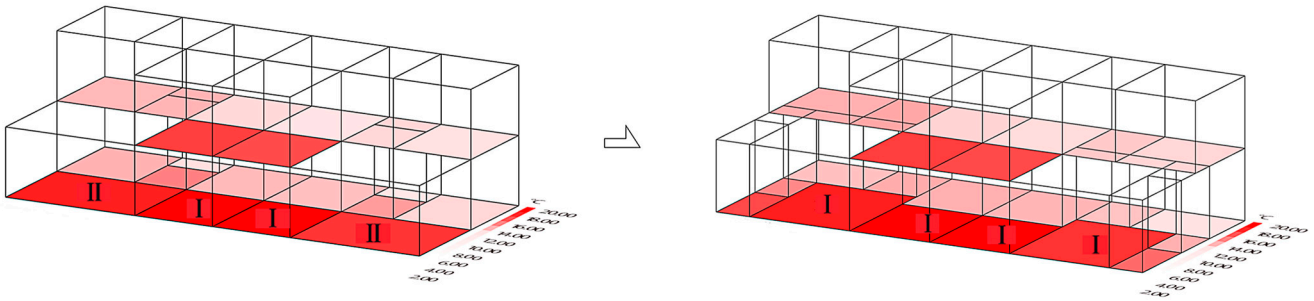


Figure 21. Distribution of indoor comfort grades before and after optimization for Construction Assembly 2.

These results demonstrate that spatial reorganization guided by the functional–thermal grading framework can independently improve winter thermal performance without changing the envelope construction. In the self-built prototype, the flexible U-shaped plan allowed auxiliary spaces to wrap the south-facing DHS effectively, resulting in nearly 40% lower heating demand and 15% higher comfort time ratio. The government-designed dwelling achieved smaller but more stable gains due to its compact and symmetric structure, confirming the robustness of the method across typologies.

The performance improvement can be attributed to three combined effects: (1) the enhanced east–west thermal buffering that mitigates edge heat loss, (2) the reduction in north-side conductive heat-loss paths by functional reallocation, and (3) the realignment of high-demand spaces into DHS zones with higher solar exposure.

Overall, functional–thermal coordination at the layout level achieved 7–40% reductions in annual heating load and 10–18% gains in heating-season comfort percentage, demonstrating the potential of spatial organization as an independent strategy for energy-resilient housing in high-altitude cold regions.

3.3. Sensitivity Analysis of Boundary-Space Parameters

Under the optimized layout baseline (Section 3.2), we assessed three boundary-space strategies—south-facing sunspace, north-facing enclosed corridor, and attic roof cavity—using a one-at-a-time (OAT) method on the self-built dwelling (Construction Assembly 1); the government-designed dwelling (Construction Assembly 2) showed the same directional trends with slightly larger load reductions, so only the key thresholds are noted to avoid redundancy. All tests used the heating season and the coldest day. These boundary spaces were selected based on preliminary heat-flow analysis, which identified the roof and the north- and south-facing façades as the main thermal exchange interfaces in Lhasa's cold season.

3.3.1. Sunspace (South-Facing)

Depth. As sunspace depth increased from 1.5 m to 3.0 m, heating load in Construction Assembly 1 increased from 6828.47 to 7066.25 kWh/a, while HSP decreased from 56.92% to 56.40%; in Construction Assembly 2, the same depth increase reduced load by 248.55 kWh/a (≈16.0%) but slightly lowered HSP (≈3.4%). The fundamental reason for these opposite trends lies in the distinct locations of the sunspace in the two prototypes. In the self-built scheme, the sunspace is attached to the ground floor, where increasing its depth directly enlarges the exterior surface area for heat loss and creates a larger, underheated volume. Conversely, in the government-designed scheme, the sunspace is added atop the roof terrace. Here, a greater depth enhances the air-layer's thermal buffer capacity and allows for more effective solar heat capture and delayed release, thereby reducing the heat loss from the main building's roof. Hence, the depth optimum lies around 2.0–2.5 m, where gains balance losses across both configurations (Figure 22).

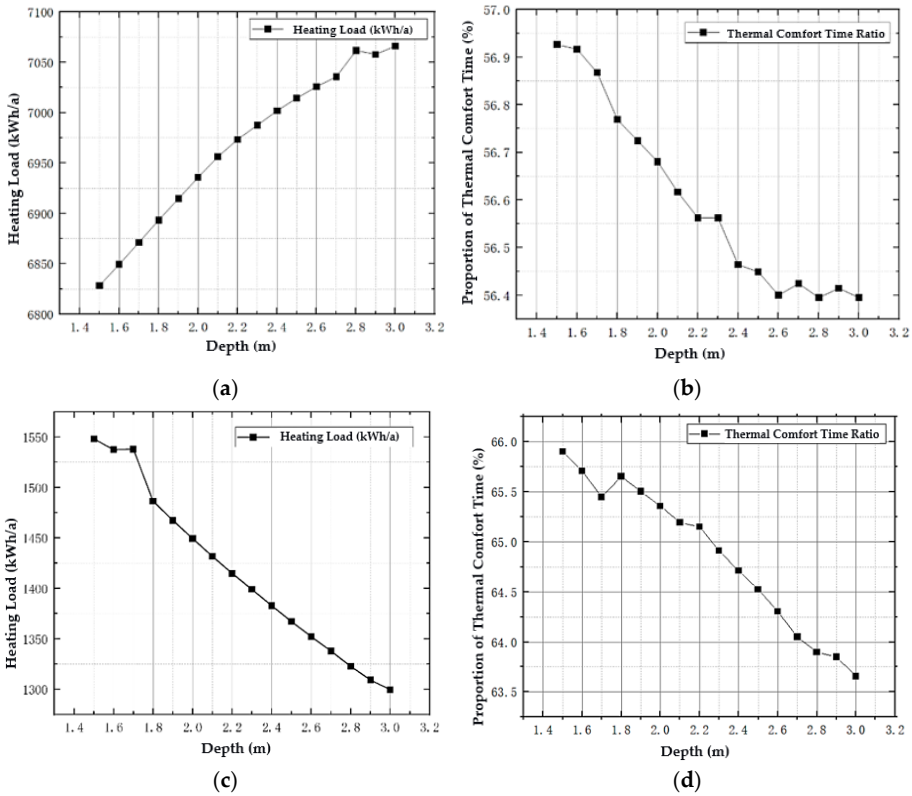
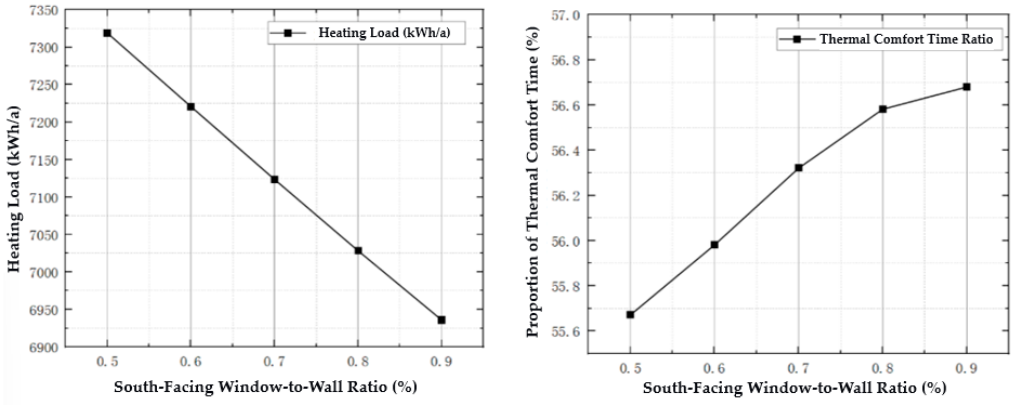


Figure 22. Effect of sunspace depth on heating performance. (**a**) Heating load and (**b**) heating-season comfort percentage (HSP) for Construction Assembly 1; (**c**) heating load and (**d**) HSP for Construction Assembly 2.

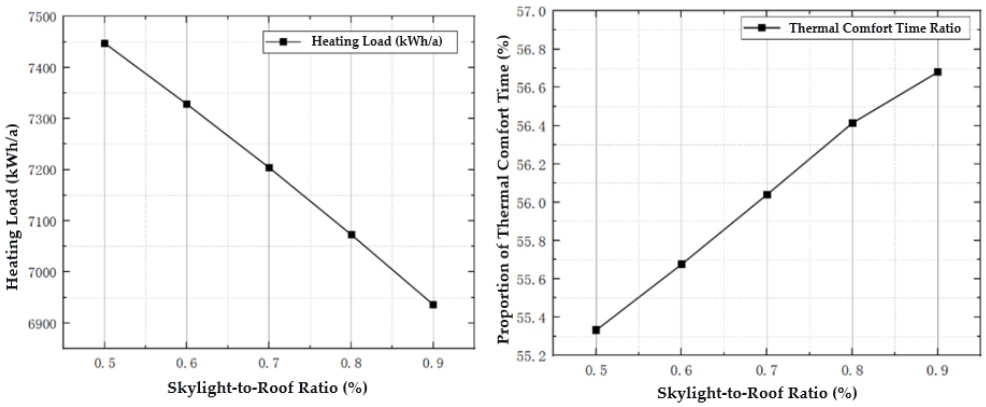
South-Facing WWR. Increasing sunspace south WWR by 10% steps (0.5→0.9) reduced heating load by ~95–100 kWh/a per step and raised HSP by ~1% per step, but incremental benefits tapered above WWR ≈ 0.8 (Figure 23). This indicates a threshold beyond which night heat loss offsets daytime gains, particularly under high-altitude radiative cooling. Therefore, WWR ≤ 0.8 is recommended.



(**a**) (**b**)

Figure 23. Effect of the south-facing window-to-wall ratio (WWR) of the sunspace on building performance. (**a**) Heating load and (**b**) HSP for Construction Assembly 1.

Skylight-to-Roof Ratio (SRR). SRR increases reduced heating load by ~111–130 kWh/a per +10%, and HSP rose by ~0.3–0.4% per +10%, yet HSP degraded when SRR exceeded ~0.10 due to intensified nocturnal losses (Figure 24). Thus, SRR ≤ 0.10 balances daylight and stability.



(**a**) (**b**)

Figure 24. Effect of the skylight-to-roof ratio (SRR) on heating performance. (**a**) Heating load and (**b**) HSP for Construction Assembly 1.

Roof slope (south-wall drop). Increasing south-wall height (reducing roof slope) raised heating load by 270.41 kWh/a across the tested range; steeper slopes (larger tilt) were closer to the winter solar altitude (≈36.6°) and captured more beam radiation, though over-steepening prompted daytime overheating and nighttime cooling, slightly lowering HSP at ~2.0 m south-wall height (Figure 25). A moderate tilt near the winter solar altitude is preferred.

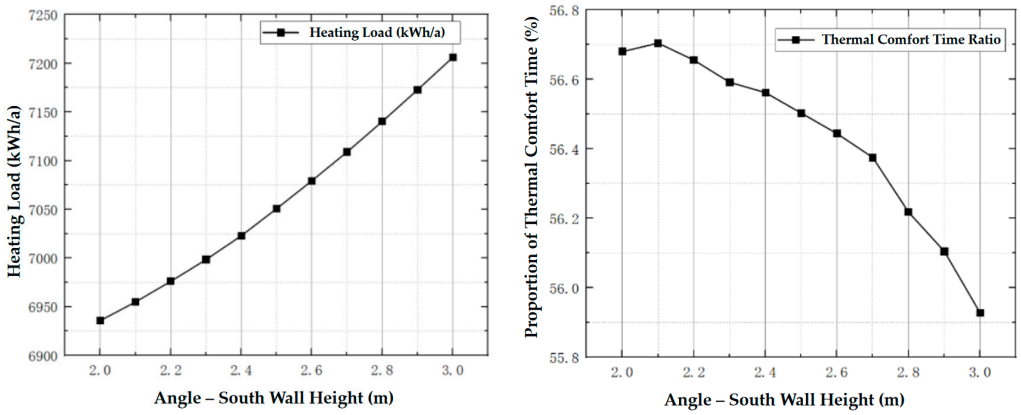


Figure 25. Effect of the sunspace roof slope, expressed by the south-wall height difference, on building performance. (**a**) Heating load and (**b**) HSP for Construction Assembly 1.

Glazing. Compared with ordinary double glazing (G1: U = 2.8 W/m^2·K, SHGC = 0.75), high-transmittance Low-E (G2: U = 1.9, SHGC = 0.47) and medium-transmittance Low-E (G3: U = 1.8, SHGC = 0.37) reduced U-value but also reduced SHGC; in winter-dominant Lhasa, the loss of solar gains dominated. Loads were lowest with G1, while G2 balanced energy and stability better than G3 (Figure 26), confirming that "solar-gain priority" outweighs insulation alone for the sunspace façade. Thus, high-transmittance Low-E is recommended where anti-condensation or comfort stability is prioritized; otherwise, clear double glazing remains competitive. The glazing properties are summarized in Table 11.

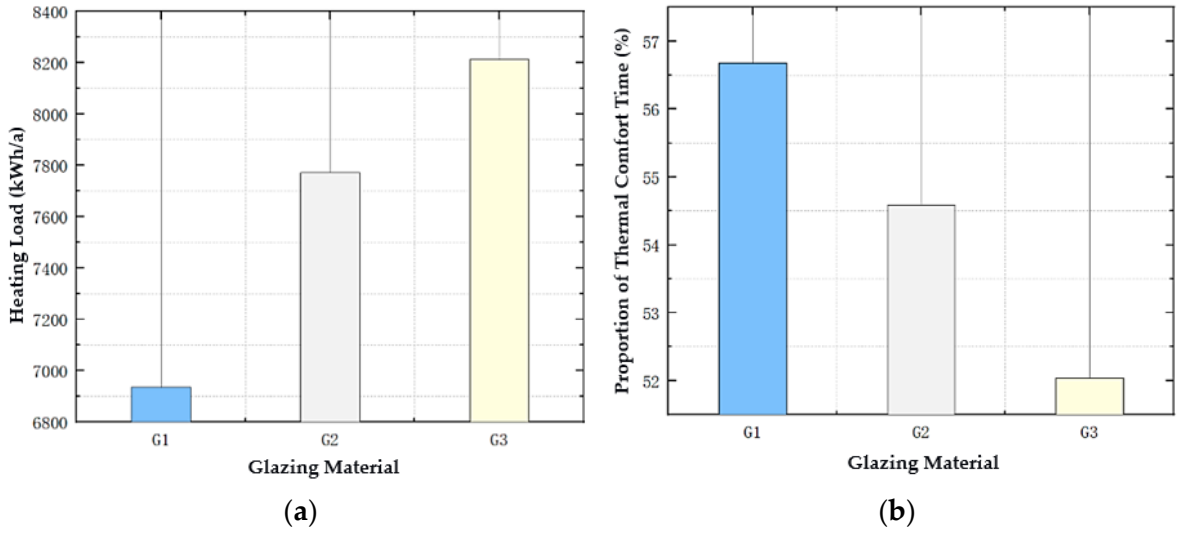


Figure 26. Effect of sunspace glazing type on heating performance. (**a**) Heating load and (**b**) HSP for Construction Assembly 1.

Table 11. Sunspace glazing options and properties (used in sensitivity tests).

ID	Make-Up	Thermal Transmittance [W/(m^2·K)]	SHGC
G1	6 clear + 12 air + 6 clear	2.8	0.75
G2	6 HT Low-E + 12 air + 6 clear	1.9	0.47
G3	6 MT Low-E + 12 air + 6 clear	1.8	0.37

Opaque materials. Sunspace wall W3 (aerated concrete, λ = 0.22) minimized load (6803.54 kWh/a), while W1 (sand-lime brick, λ = 1.10) maximized it; however, W2 (fly-ash

brick) slightly improved HSP due to higher heat capacity (ρ·C), smoothing diurnal swings (Figure 27). Floor F3 (fly-ash ceramsite, λ = 0.44) yielded the lowest load (6520.41 kWh/a), whereas the higher-capacity F1 (gravel concrete) achieved the highest HSP (Figure 28). Thus, "insulation for load, capacity for comfort" governed opaque choices.

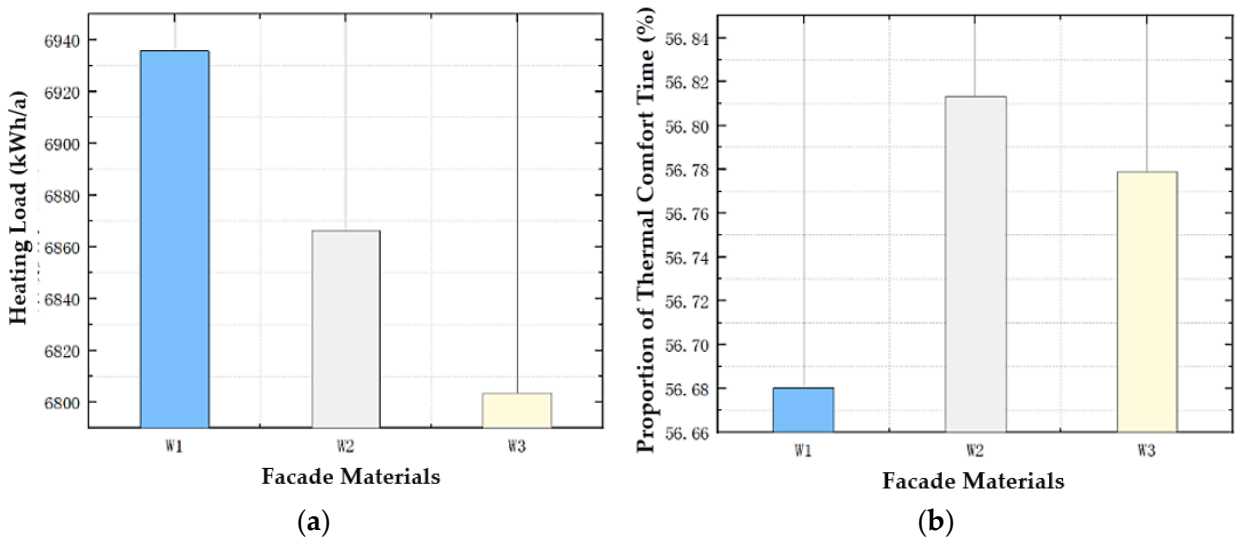


Figure 27. Effect of sunspace wall materials on building performance. (**a**) Heating load and **(b)** HSP.

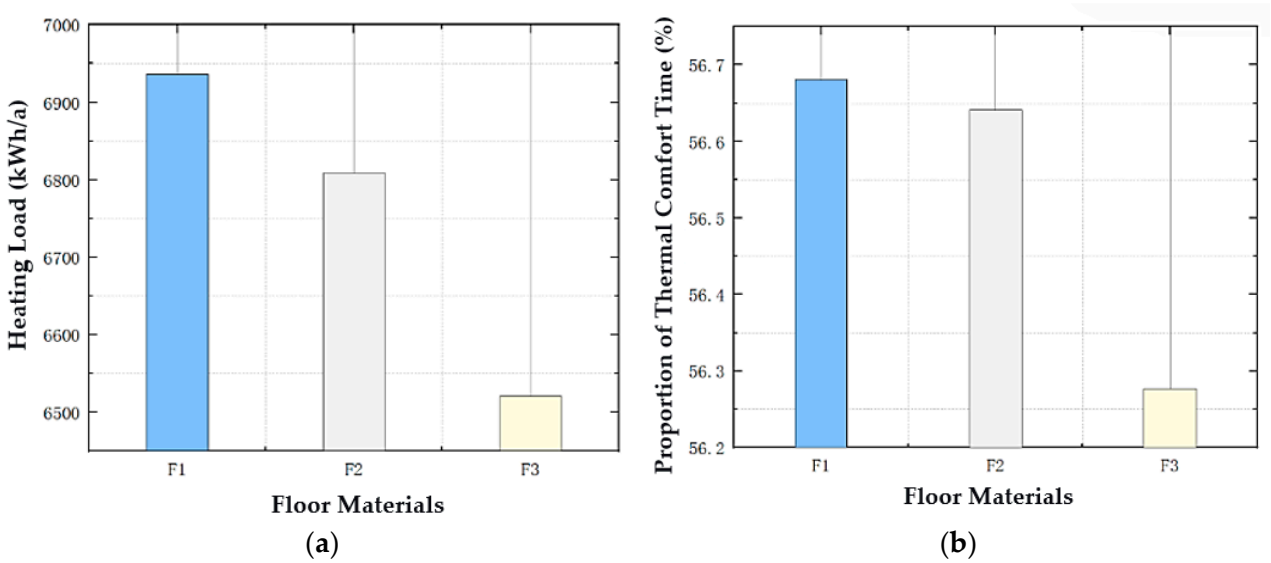
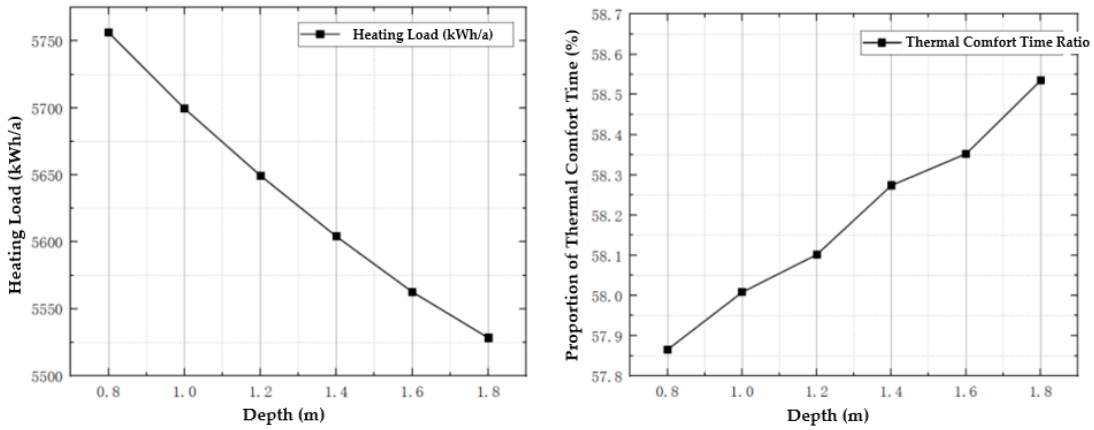


Figure 28. Effect of sunspace floor materials on building performance. (**a**) Heating load and (**b**) HSP.

3.3.2. North-Facing Enclosed Corridor

Depth. Increasing corridor depth from 0.8 m to 1.8 m decreased heating load by ~50–60 kWh/a per +0.2 m and raised HSP by 0.67% in total, reflecting reduced north loss and improved air-layer buffering (Figure 29). Beyond ~2.0 m, gains fell below ≈2%, suggesting diminishing returns. Therefore, a corridor depth of 1.5–2.0 m is sufficient.

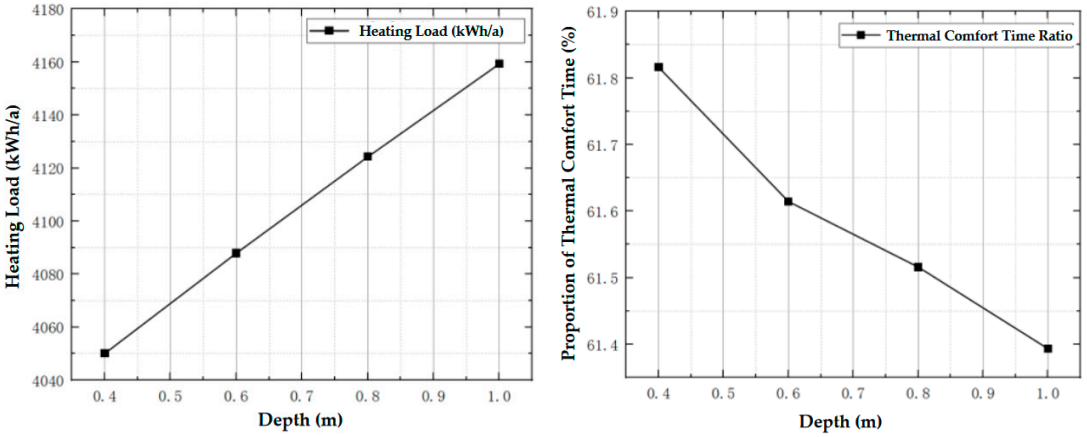


(**a**) (**b**)

Figure 29. Effect of north-facing enclosed corridor depth on building performance. (**a**) Heating load and (**b**) HSP for Construction Assembly 1.

3.3.3. Attic Roof Cavity

Cavity height and insulation. Raising attic cavity height from 0.4 m to 1.0 m slightly increased load (4050.12 → 4159.35 kWh/a) and reduced HSP by ~0.43%, likely due to greater surface area and natural convection within the cavity when too tall; however, a cavity ≥ ~2.0 m stabilizes top-floor night temperature in the full-height variant tested elsewhere. Insulation showed monotonic benefits with a practical knee at ~150 mm, beyond which extra savings were <2% (Figure 30). Thus, prioritize ~150 mm insulation and avoid over-tall cavities unless needed for a ventilation strategy.



(**a**) (**b**)

Figure 30. Effect of attic cavity parameters on building performance. (**a**) Variation in heating load with cavity height; (**b**) variation in heating load with insulation thickness for Construction Assembly 1.

3.3.4. Sensitivity Ranking and Design Thresholds

Across all parameters, sunspace-related variables dominate sensitivity for both heating load and HSP, while the north corridor provides steady but smaller benefits and the attic cavity is primarily an insulation question. Table 12 consolidates the sign of influence, the key threshold identified in this study, and a practical design priority for multi-objective optimization in Section 3.5. Heating load and HSP originate from the same deterministic model and therefore co-vary as complementary expressions of winter thermal performance.

Table 12. Consolidated sensitivity and thresholds for boundary-space parameters (Construction Assembly 1; Assembly 2 shows the same trends with slightly larger load reductions).

Category	Parameter	Trend (Load)	Key Threshold (This Study)	HSP Effect (Qual.)	Design Priority
Sunspace	Depth	↑ (Assembly 1); ↓ (Assembly 2 rooftop case)	2.0–2.5 m	slight ↓ at extremes	High
	South-facing WWR	↓ (until loss penalty)	≤0.8 (use high-transmittance glazing where needed)	↑ to ~+1%/10% step, then taper	High
	SRR (skylight-to-roof)	↓ (to a point)	≤0.10	↑ then ↓ beyond ~0.10	High
	Roof slope (tilt)	↓ when tilted toward winter altitude; ↑ if too flat	Moderate tilt near winter solar altitude (~36.6°)	stable if not over-steep	Medium
	Glazing type	depends on U vs. SHGC	High-transmittance Low-E or clear double (solar-gain priority)	stability ↑ with Low-E	High
	Wall material	↓ with lower λ	Low-λ wall (e.g., aerated concrete)	capacity can aid HSP	Medium
	Floor material	↓ with lower λ	Low-λ floor (e.g., fly-ash ceramsite)	high capacity improves HSP	Medium
Corridor	Depth	↓ with diminishing returns	1.5–2.0 m	slight ↑	Medium
Attic	Insulation thickness	↓ (monotonic)	≈ 150 mm (knee)	slight ↑	Medium
	Cavity height	slight ↑ if too tall	Moderate (avoid excessive height)	slight ↓ if too tall	Low–Medium

Note: Arrows (↑/↓) indicate qualitative trends of heating load within tested ranges, not global monotonicity beyond them. ("Trend" indicates the direction of change in heating load as the parameter increases within the tested range. Thresholds are the recommended bounds beyond which marginal gains diminish or comfort penalties emerge).

Follow-on guidance. For Section 3.5, we fix the decision bounds at sunspace depth 2.0–2.5 m, south WWR $\leq$ 0.8, SRR $\leq$ 0.10, high-transmittance Low-E (or clear double glazing where solar-gain priority dominates), corridor depth 1.5–2.0 m, and roof insulation $\approx$ 150 mm with a moderate attic cavity height.

3.4. Multi-Objective Optimization Results

Building on the sensitivity outcomes in Section 3.4, we selected all the initially chosen parameters as decision variables and ran a bi-objective NSGA-II (minimize heating load; maximize HSP) under the unified baseline in Section 2. The algorithm was configured with a population of 50, 20 generations, a crossover rate of 0.9, and default mutation, consistent with the convergence evidence reported below. Both models were analyzed as Construction Assembly 1 (self-built scheme) and Construction Assembly 2 (government-designed scheme). The following reports results and interpretation together.

3.4.1. Convergence Behavior and Search Quality

For Construction Assembly 1, the standard deviation of heating load decreased from 592.74 to 90.80, while the HSP deviation dropped from 0.0457 to 0.0026. For Construction Assembly 2, the corresponding reductions were 385.64 to ≈80.00 for heating load, and 0.0406 to 0.00406 for HSP. Both curves flattened after approximately the 20th generation, as shown in Figures 31 and 32, indicating stable convergence.

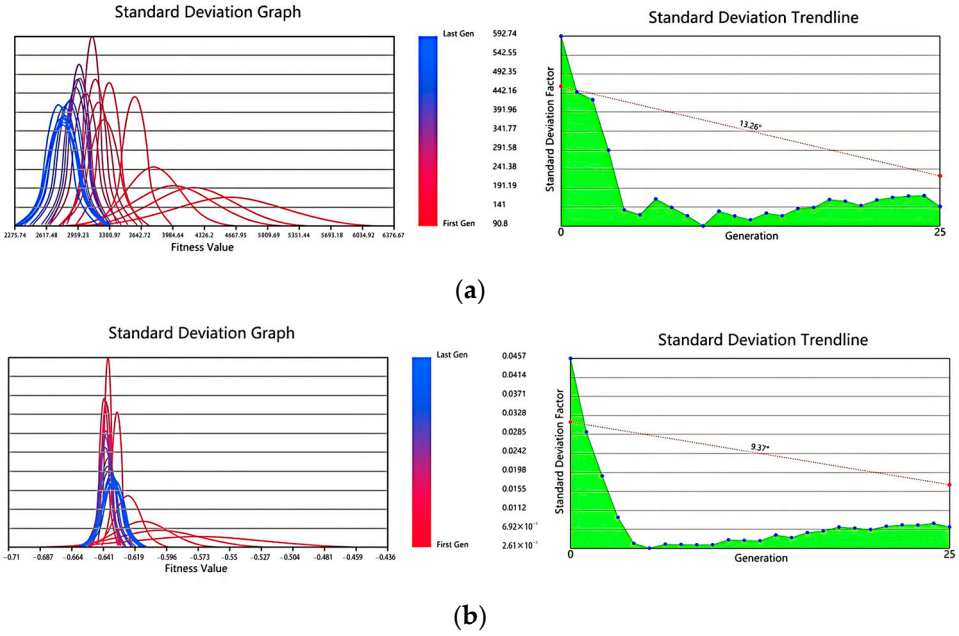


Figure 31. Convergence statistics for Construction Assembly 1: (**a**) standard deviation of heating load per generation; (**b**) standard deviation of HSP per generation.

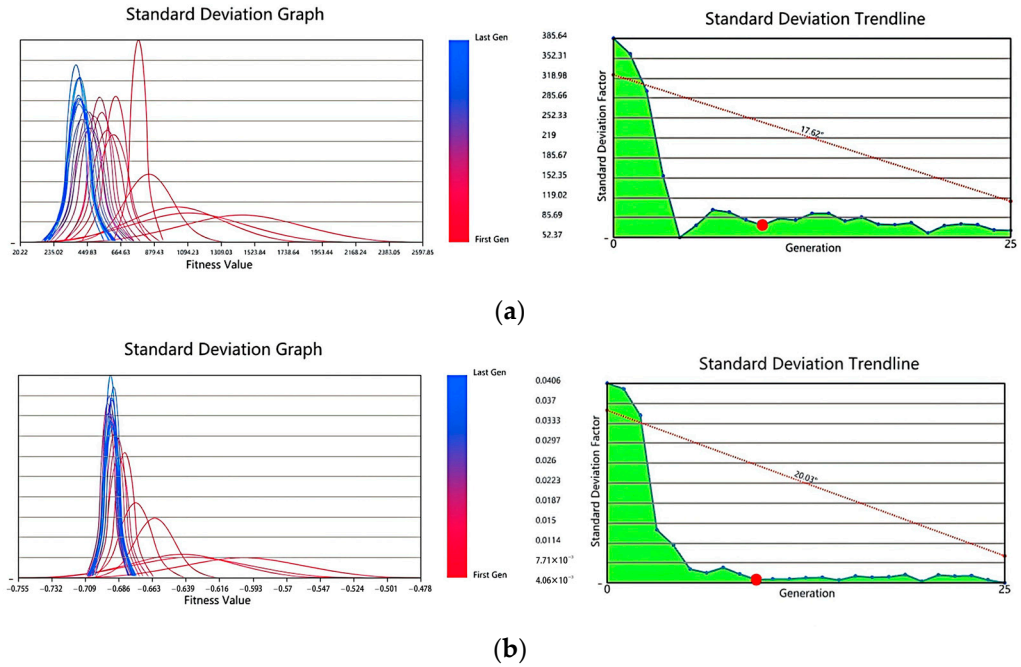


Figure 32. Convergence statistics for Construction Assembly 2: (**a**) standard deviation of heating load per generation; (**b**) standard deviation of HSP per generation.

The rapid early decline followed by a low-amplitude plateau demonstrates the effective sorting and diversity control of NSGA-II, with the population converging toward the

Pareto front. In conclusion, optimization reached stable convergence by the 20th generation, and the solution populations achieved statistical stability.

3.4.2. Pareto Fronts and Comparative Potential

The Pareto front of Construction Assembly 2 was located in a region with simultaneously higher HSP and lower heating load compared to that of Assembly 1, demonstrating its greater potential for passive performance enhancement (Figure 33).

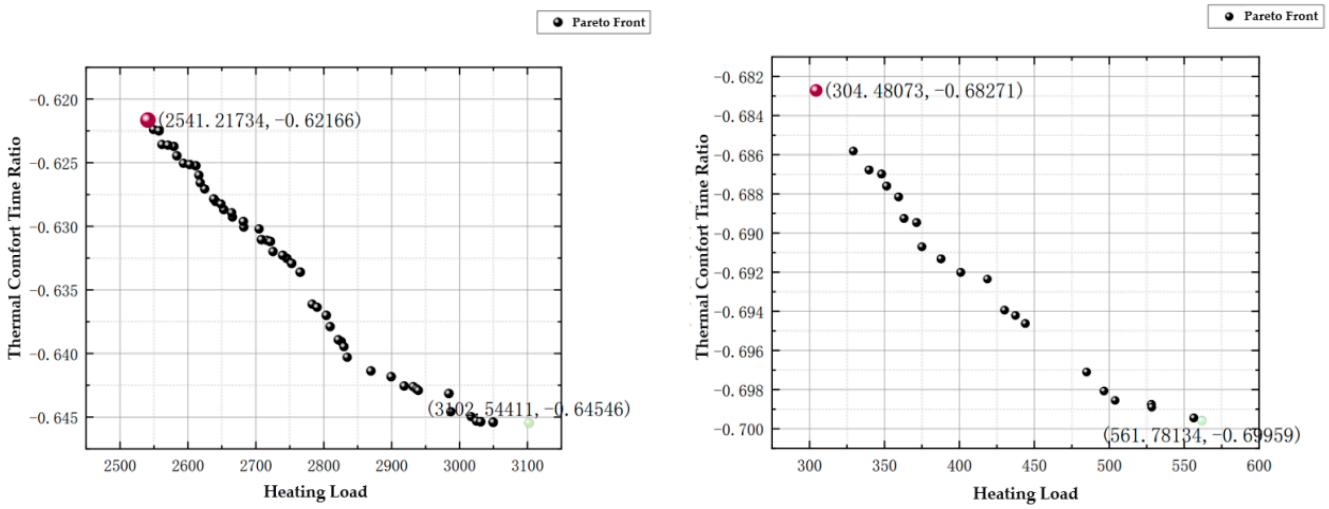


Figure 33. Final-generation Pareto fronts and representative solutions: (**a**) Construction Assembly 1 with marked energy-minimum, comfort-maximum, and compromise points; (**b**) Construction Assembly 2 with the same markings.

This difference derives from their sunspace configurations: the ground-attached sunspace (Assembly 1) amplifies heat-loss area and under-heated volume as it deepens, while the rooftop sunspace (Assembly 2) enhances solar capture and delayed release through its larger air-layer capacity. Both assemblies exhibited converged Pareto fronts trending toward simultaneous load reduction and comfort enhancement.

3.4.3. Compromise Solutions and Optimization Outcomes

Using the Euclidean-distance-to-ideal-point method, representative optimal solutions were identified from the final Pareto sets (see Table 13). For Construction Assembly 1, the compromise solution achieved a heating load of 2541.22 kWh/a with an HSP of 62.17%, while comfort-oriented solutions yielded higher HSP (around 64.55%) at the cost of significantly increased energy consumption (over 3000 kWh/a).

Table 13. Representative Pareto-optimal solutions (final generation).

Prototype Type	Optimal Solution ID (Gen, Idv)	Heating Load (kWh/a)	HSP (%)	Selection Basis (Euclidean Distance)
Self-built	Gen19, Idv3	2541.22	62.17	Compromise (Euclidean distance)
	Gen14, Idv1	3102.54	64.55	Comfort optimum
	Gen12, Idv24	3049.68	64.54	Near-comfort optimum
Government	Gen19, Idv0	304.48	68.27	Compromise (Euclidean distance)
	Gen19, Idv1	561.78	69.96	Comfort optimum

A similar trade-off was observed for Construction Assembly 2, whose compromise solution operated at a much lower energy level (304.48 kWh/a) and a higher comfort level (68.27%), while the comfort optimum required 561.78 kWh/a to reach 69.96%. This contrast underscores its superior passive performance compared with the self-built type.

3.4.4. Decision Patterns in the Compromise Set

Analysis of the parameter values in the compromise solutions revealed several consistent design patterns: (1) Strong solar gain—south-facing WWR and SRR were relatively high but limited to $\leq$0.8 and $\leq$0.10, respectively; (2) Roof tilt aligned with the winter solar altitude (~36°); (3) North buffer depth around 1.5–2.0 m providing stable thermal resistance; (4) Opaque envelope pairing low λ insulation with moderate thermal capacity.

In Assembly 1, the ground-attached sunspace performed best with a shallower optimal depth (1.5 m), minimizing external heat loss; while in Assembly 2, the rooftop sunspace favored a deeper configuration (2.9 m) to enhance heat storage and delayed release.

These configurations synchronize daytime solar gain and nighttime temperature stability, transforming the DHS–LBS gradient into an adaptive buffering system. The optimized schemes maintained nearly identical building volumes and shape coefficients, ensuring practical constructability. Although both achieved substantial performance gains, their heating loads remain higher than ultra-low-energy benchmarks, suggesting further potential for envelope optimization.

3.5. Optimized Schemes and Performance Improvements

Building upon the multi-objective optimization results in Section 3.5, this section quantitatively compares the optimized schemes of Construction Assembly 1 (self-built dwelling) and Construction Assembly 2 (government-designed dwelling) with their respective baseline and layout-optimized models. The analysis focuses on heating load, heating-season comfort percentage (HSP), and the spatial thermal characteristics of the optimized configurations.

3.5.1. Energy and Comfort Gains

For Construction Assembly 1 (self-built dwelling), the fully optimized model achieved a heating load of 2541.22 kWh/a, representing a 79.6% reduction compared with the baseline case (12,465.81 kWh/a), and a 66.6% reduction compared with the layout-optimized case (7611.70 kWh/a), as shown in Figure 34a. The HSP improved to 62.17%, an increase of 31.22 percentage points (≈50.2%) over the baseline (30.95%) and 26.47 percentage points (≈42.6%) over the layout-optimized model (35.7%), consistent with the values summarized in Table 14.

For Construction Assembly 2 (government-designed dwelling), the final optimized scheme (with all optimal boundary-space parameters applied to the full duplex model) yielded a heating load of 815.53 kWh/a, corresponding to an 87.7% reduction compared with the baseline (6631.39 kWh/a) and an 86.7% reduction compared with the layout-optimized model (6152.62 kWh/a), as illustrated in Figure 34b. Its HSP rose to 69.65%, showing a 54.1% gain over the baseline (32.0%) and a 45.8% gain relative to the layout-optimized scheme (37.73%). This value differs from the compromise solution reported in Section 3.5 (304.48 kWh/a) because the latter represents a single Pareto individual, whereas the present result reflects the performance of the complete two-unit model after reintegrating all optimized parameters.

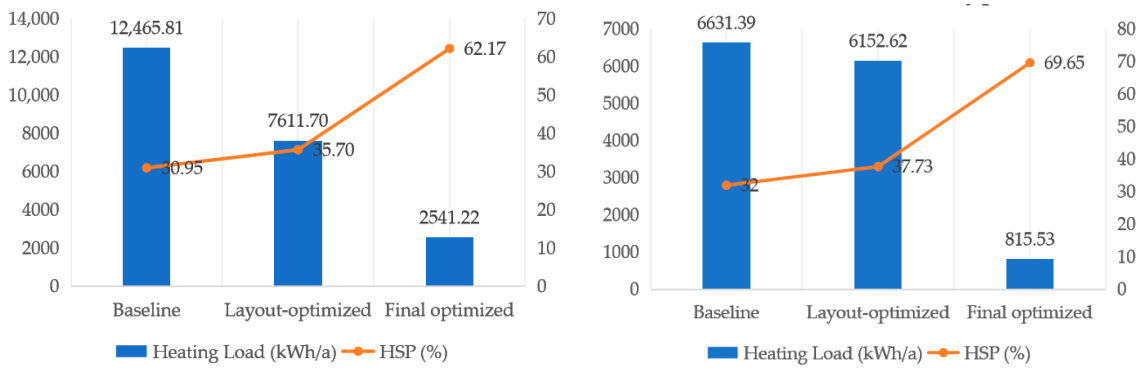


Figure 34. Heating load and HSP across optimization stages for two prototypes: (**a**) Self-built prototype. (**b**) Government prototype.

Table 14. Summary of performance improvements in optimized schemes.

Prototype	Scheme Stage	Heating Load (kWh/a)	Energy-Saving Rate (vs. Baseline)	HSP (%)	Improvement Rate (vs. Baseline)
Self-built	Baseline	12,465.81	–	30.95	–
	Layout-optimized	7611.70	38.93%	35.70	15.35%
	Final optimized	2541.22	79.61%	62.17	50.20%
Government	Baseline	6631.39	–	32.00	–
	Layout-optimized	6152.62	7.22%	37.73	17.90%
	Final optimized	815.53 *	87.70%	69.65	54.06%

* Note: For the government-designed dwelling, the final optimized load (815.53 kWh/a) was calculated for the complete two-unit model after reintegrating all optimized boundary-space parameters, whereas the Pareto solutions in Section 3.5 refer to single-unit results.

These results demonstrate that coupling spatial reconfiguration with thermal-buffer boundary design produces a synergistic improvement—simultaneously lowering energy demand and enhancing thermal comfort beyond what either strategy can achieve alone.

3.5.2. Thermal Distribution and Spatial Improvement

After integrating the optimized boundary-space parameters, the spatial configuration of both assemblies exhibited a characteristic and effective "multi-directional thermal enclosure" pattern.

In Construction Assembly 1, as shown in Figures 35a and 36a, ancillary rooms were added around the core living zone, forming a south-facing sunspace, north enclosed corridor, and east–west auxiliary rooms. The south sunspace absorbed solar radiation through transparent enclosures and transferred heat indoors via convection and radiation, while the north corridor and attic cavity effectively suppressed heat loss. As a result, the indoor temperature gradient between DHS and LBS was reduced by 2–3 °C, and the main functional spaces were upgraded from acceptable (Grade II–III) to comfortable (Grade I) levels, according to the adaptive thermal comfort criteria.

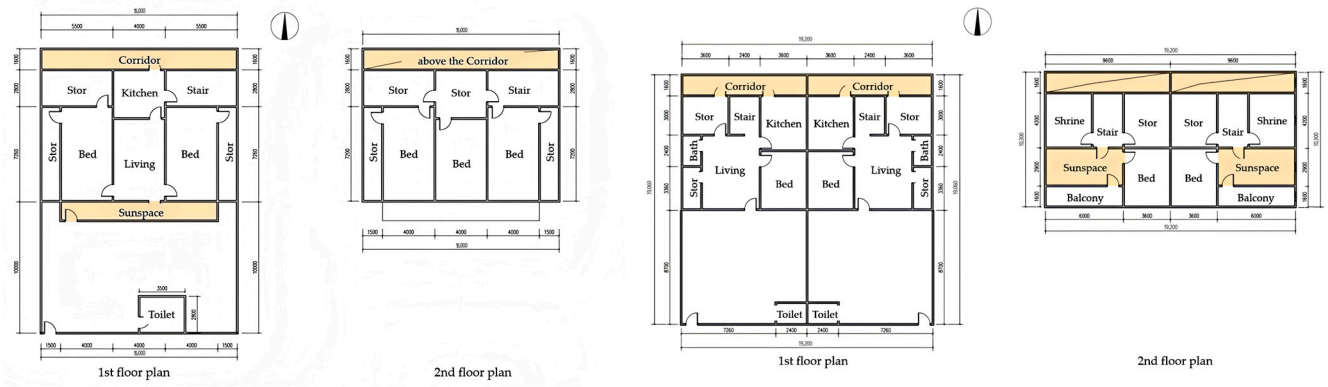


Figure 35. Optimized floor plans: (**a**) self-built dwelling; (**b**) government-designed dwelling.

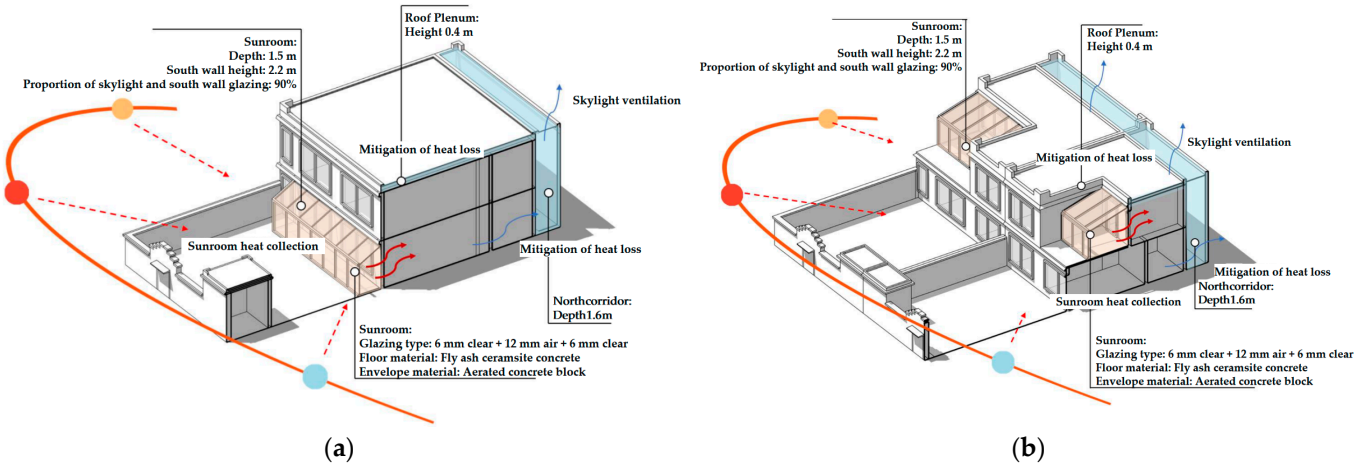


Figure 36. Schematic of optimized boundary-space configuration and thermal-flow mechanisms: (**a**) self-built vernacular housing; (**b**) government-designed resettlement housing.

In Construction Assembly 2, as shown in Figures 35b and 36b, a roof-terrace sunspace was added above the first floor, paired with north enclosed corridors and attic insulation layers. These additions improved both horizontal and vertical heat buffering, maintaining higher mean indoor temperatures and more uniform distribution across floors. The thermal field stabilized with smaller diurnal swings, aligning with the comfort gains summarized in Table 14.

3.5.3. Validation and Discussion

Model validation in Section 2.5 indicated that the simulation error between measured and simulated indoor temperatures remained within ±5%. This consistency confirms the reliability of the optimization outcomes.

Comparing both assemblies, Construction Assembly 1 demonstrated significant relative improvement due to its initially poor baseline thermal performance, whereas Construction Assembly 2 exhibited higher absolute efficiency and comfort stability due to superior form compactness and integrated terrace design. These findings verify that the integrated optimization of spatial layout and boundary-space parameters provides an effective passive design path for high-altitude cold regions.

4. Conclusions

This study developed and validated an integrated optimization framework to enhance the winter thermal performance of new-type vernacular housing in high-altitude,

cold regions, using Lhasa as a case study. The research demonstrates that a coordinated strategy, synergistically combining spatial hierarchy reorganization with boundary-space optimization within a parametric workflow, can achieve substantial energy savings and comfort improvements through purely passive means. The principal findings lead to several key conclusions.

The study confirms the high efficacy of the coupled spatial and boundary-layer enhancement strategy. For the self-built and government-designed prototypes, heating loads were reduced by 79.6% and 87.7%, respectively, while the heating-season comfort percentage (HSP) increased by 50.2% and 54.1%. These significant gains are attributed to the synergistic operation of sunspaces, north buffer corridors, and attic cavities, which collectively reshape the DHS–LBS temperature gradient into a stable, multi-directional thermal enclosure system.

Furthermore, the sensitivity and multi-objective optimization analyses yielded a set of quantifiable parameters for schematic design. These include a sunspace depth of 2.0–2.5 m, a south-facing window-to-wall ratio (WWR) ≤ 0.8, a skylight-to-roof ratio ≤ 0.10, a north-corridor depth of 1.5–2.0 m, and roof insulation of approximately 150 mm. While derived from the Lhasa context, these thresholds offer a transferable foundation for other high-altitude, solar-rich cold climates, subject to local calibration.

An equally important conclusion is the straightforward economic and construction feasibility of the proposed strategy. The optimization outcomes—such as the recommended sunspace depth (2.0–2.5 m), north corridor width (1.5–2.0 m), and standard roof insulation (150 mm)—leverage locally prevalent construction techniques and materials (e.g., stone masonry, concrete blocks, standard glazing). This ensures that the enhanced performance does not rely on expensive or imported technologies, making the strategy highly suitable for widespread application, including in resettlement housing projects. The results demonstrate that this form of early-stage spatial and boundary optimization, rather than post-design envelope reinforcement alone, offers a more cost-effective and constructible pathway to low-energy comfort housing. Therefore, quantitative design logic and thresholds can be directly incorporated into regional building codes or assessment tools during the design phase, providing new ideas for ongoing "comfortable housing projects" and similar initiatives.

Finally, the research provides quantifiable guidance for design practice and policy, demonstrating that prioritizing spatial and boundary optimization in the early design stage is more effective than retrofitting insulation post-design. The performance indicators and design logic can be integrated into regional building standards to promote passive, climate-adaptive design. Despite the primary focus on winter performance, which presents a limitation for summer behavior, and the exclusion of internal heat gains to isolate passive performance, which may lead to an overestimation of absolute heating loads, the study also did not address psychological or mood-related factors affecting thermal perception. Additionally, the models assumed an open-sky condition without shading from surrounding buildings, which is representative of the low-density rural context studied but may not hold for denser settlement planning. The methodological framework is broadly applicable. Future work should expand to multi-seasonal analysis and post-occupancy validation. In summary, this work outlines an economically viable pathway toward resilient, low-energy housing in cold, high-altitude environments. The significantly improved passive thermal performance not only addresses current energy and comfort issues but also inherently enhances the building's resilience to future climate uncertainties, such as more severe winter conditions or energy supply disruptions, without increasing mechanical system dependency.

Author Contributions: Conceptualization, X.M. and Z.M.; methodology, X.M. and Z.M.; software, X.M. and Z.M.; validation, X.M.; formal analysis, X.M.; investigation, X.M. and Z.M.; resources, Z.M.; data curation, X.M. and Z.M.; writing—original draft preparation, X.M. and Z.M.; writing—review and editing, X.M.; visualization, H.X.; supervision, H.X.; project administration, H.X.; funding acquisition, H.X. All authors have read and agreed to the published version of the manuscript.

Funding: This research was supported by the Sichuan Provincial Department of Science and Technology (No. 2023YFQ0048).

Data Availability Statement: The climate dataset (EPW files) used in this study is publicly available at https://energyplus.net/weather (accessed on October 2024). Simulation data generated during the study are available from the corresponding author upon reasonable request.

Conflicts of Interest: The authors declare no conflicts of interest.

References

1. Tsinghua University Building Energy Research Center. *Annual Report on China Building Energy Efficiency 2025*; Tsinghua University Press: Beijing, China, 2025. (In Chinese)
2. Central People's Government of the People's Republic of China. New Countryside, New Plateau: A Review of the "11th Five-Year Plan" Settlement Project in Tibet Autonomous Region. Available online: https://www.gov.cn/gzdt/2010-12/07/content_1760686.htm (accessed on 31 October 2025). (In Chinese)
3. People's Government of Tibet Autonomous Region. Conference on the Construction of Settlements for Farmers and Herders in the Entire Region Convened. Available online: https://www.xizang.gov.cn/xwzx_406/bmkx/201812/t20181216_17779.html (accessed on 31 October 2025). (In Chinese)
4. National Development and Reform Commission (NDRC). Notice on Issuing the "13th Five-Year Plan Period Poverty Alleviation and Relocation Work Plan". Available online: https://www.waizi.org.cn/law/13276.html (accessed on 31 October 2025). (In Chinese).
5. State Council Information Office of the People's Republic of China. *White Paper on Peaceful Liberation and Prosperous Development of Tibet*; State Council Information Office: Beijing, China, 2021. (In Chinese)
6. Liu, Y.; Hu, X.; Zhou, Y.; Wang, J. Analysis of Factors Influencing Indoor Thermal Environment in Lhasa's New Vernacular Dwellings in Winter. *J. Xi'an Univ. Archit. Technol. (Nat. Sci. Ed.)* **2019**, *51*, 109–115. (In Chinese) [CrossRef]
7. He, Q.; Gao, H.; Liu, D.; Zhu, X. Study on Energy-Saving Optimization of Traditional Dwellings in Lhasa. *Archit. Cult.* **2019**, *15*, 241–243. (In Chinese) [CrossRef]
8. Huang, L.; Deng, C.; Lan, B. Comparative Analysis of Indoor Thermal Environment in Traditional and New Vernacular Dwellings in Lhasa Rural Areas in Winter. *Build. Sci.* **2012**, *28*, 61–66. (In Chinese) [CrossRef]
9. *ANSI/ASHRAE Standard 55*; Thermal Environmental Conditions for Human Occupancy. ASHRAE: Atlanta, GA, USA, 2020.
10. *ISO 7730:2005*; Ergonomics of the Thermal Environment—Analytical Determination and Interpretation of Thermal Comfort Using Calculation of the PMV and PPD Indices and Local Thermal Comfort Criteria. ISO: Geneva, Switzerland, 2005.
11. Zhao, Q.; Xie, Y.; Li, Z. Thermal Performance Requirements for Wall Structures of Vernacular Dwellings in Lhasa Area. *Hous. Sci.* **2021**, *41*, 51–57. (In Chinese) [CrossRef]
12. Wang, Q. The Optimization of the Insulation and Heat Storage of Rural Residential Building Envelope in Lhasa Region. Master's Thesis, Xi'an University of Architecture and Technology, Xi'an, China, 2017. (In Chinese).
13. Dai, Q. Performance-Oriented Extraction and Reconstruction of Residential Forms in Lhesa. Master's Thesis, Xi'an University of Architecture and Technology, Xi'an, China, 2024. (In Chinese). [CrossRef]
14. Liu, Z.; Wu, D.; Li, J.; Liu, Y.; Hao, A. Optimizing Building Envelope Dimensions for Passive Solar Houses in the Qinghai-Tibetan Region: Window-to-Wall Ratio and Depth of Sunspace. *J. Therm. Sci.* **2019**, *28*, 1115–1128. [CrossRef]
15. Editorial Board of Master Series. *The Works and Ideas of Thomas Herzog*; China Electric Power Press: Beijing, China, 2006.
16. Han, P.; Mei, H. Ecological Design on Buffer Cavity of Buildings in Cold Region. *Architect* **2015**, 56–65. Available online: https://kns.cnki.net/kcms2/article/abstract?v=BVV9sVd_tjEWcE6Cq6L4SyovLYPyiu_Q5-Nucr6wbLUSz2nlaWGEVeZSQ-4F1TjewgQP-1Jmy0uYZ-e3qokdEwHJ5ANa8wW28Frfv-1G1_bgl0WJ3K4l3fDumBl-5-UgSAiwszSBfmCoDVzhj4M1asLHpIeqcDjAhLtXGr_aSSw=&uniplatform=NZKPT (accessed on 22 November 2025). (In Chinese).
17. Liu, Y.; Yu, Z.; Song, C.; Wang, D. Heating Load Reduction Characteristics of Passive Solar Buildings in Tibet, China. *Build. Simul.* **2022**, *15*, 975–994. [CrossRef]
18. Huang, L.; Kang, J. Thermal Comfort in Winter Incorporating Solar Radiation Effects at High Altitudes—Case of Lhasa. *Build. Simul.* **2021**, *14*, 1633–1650. [CrossRef]

19. Singh, M.K.; Mahapatra, S.; Atreya, S.K. Thermal Comfort Study of Himalayas in India: A Comparative Analysis of Traditional and Modern Houses. *Build. Environ.* **2019**, *151*, 211–223. [CrossRef]
20. Mazzaglia, N.; Ochoa, C.E.; Caicedo, D.; Leiva, C.; Figueroa, R. On the Passive Cooling and Thermal Comfort in Buildings in the Andean Highlands of Ecuador. *Energy Build.* **2021**, *231*, 110597. [CrossRef]
21. Albatayneh, A. Optimising the Parameters of a Building Envelope in the East Mediterranean Saharan, Cool Climate Zone. *Buildings* **2021**, *11*, 43. [CrossRef]
22. Liu, B.; Liu, Y.; Xin, Q.; Kou, X.; Song, J. Energy-Efficient Design of Immigrant Resettlement Housing in Qinghai: Solar Energy Utilization, Sunspace Temperature Control, and Envelope Optimization. *Buildings* **2025**, *15*, 1434. [CrossRef]
23. Yang, Q.; Xu, F.; Lu, W.; Yang, Z.; Bai, Y.; Wen, B. Green Renovation and Multi-Objective Optimization of Tibetan Courtyard Dwellings. *Build. Environ.* **2025**, *279*, 113071. [CrossRef]
24. *GB 50176-2016*; Code for Thermal Design of Civil Buildings. China Architecture & Building Press: Beijing, China, 2016. (In Chinese)
25. Chen, L. Energy-Saving Design Methods for Rural Residential Buildings in the U-Tsang Region Based on Architectural Form. Master's Thesis, Xi'an University of Architecture and Technology, Xi'an, China, 2021. (In Chinese). [CrossRef]
26. Zhen, H. Research on the Architectural Evolution of Tibetan Vernacular Dwellings in Lhasa after the Founding of the People's Republic of China. Master's Thesis, Xi'an University of Architecture and Technology, Xi'an, China, 2021. (In Chinese). [CrossRef]
27. Huang, L.; Hamza, N.; Lan, B.; Zuo, J. Climate-Responsive Design of Traditional Dwellings in the Cold-Arid Regions of Tibet and a Field Investigation of Indoor Environments in Winter. *Energy Build.* **2016**, *128*, 697–712. [CrossRef]
28. *GB 50736-2012*; Design Code for Heating, Ventilation and Air Conditioning of Civil Buildings. Ministry of Housing and Urban-Rural Development of the People's Republic of China: Beijing, China, 2012. (In Chinese)
29. Chen, L. Research on the Design of Courtyard-Style Dwellings in Lhasa Based on Solar Radiation Heat Utilization. Master's Thesis, Xi'an University of Architecture and Technology, Xi'an, China, 2022. (In Chinese). [CrossRef]
30. Yao, H.; Wang, H.; Wu, Y.; Li, J. Experimental Study on the Design Application Prioritizing Solar Radiation Heat Utilization in Courtyard-Style Dwellings in Lhasa. *Archit. Technol.* **2022**, *28*, 80–83. (In Chinese) [CrossRef]
31. Sun, K. Integration of Green Building Design Concepts in Architectural Engineering Design. *Policy Res. Explor.* **2020**, *27*. Available online: https://kns.cnki.net/kcms2/article/abstract?v=BVV9sVd_tjHR-KF46yrtj747aiCeaNJyEI7mQa0kH7nyINn1RldIpJXfqB5aIVlJoztCGGrHTKwIOUS1FL4KeZjt5EHR6VPbpiHCUD9a1zS_YQxlwhko6MY5jVYNLdwzSlLlumXGoM4504I3w19gNF9YtJzF1CKeiZW8CvKo8qA=&uniplatform=NZKPT (accessed on 22 November 2025). (In Chinese).
32. Liu, J.; Wu, L. New Energy utilization in Architectural Energy Conservation and Design. *Energy Eng.* **2001**, *2*, 12–15. (In Chinese) [CrossRef]
33. Song, W. Research on Design Strategies for Building Composite Interfaces Based on Spatial Thermal Buffer Effects. Master's Thesis, Southeast University, Nanjing, China, 2019. (In Chinese). [CrossRef]
34. Chen, S. Analysis of Architectural Spatial Hierarchy and Its Constructive Expression. Master's Thesis, Dalian University of Technology, Dalian, China, 2017. (In Chinese).
35. Ma, C.; Liu, Y.; Wang, D.; Gao, Y. Analysis of Thermal Performance and Energy-Saving Strategies for Rural Residential Buildings in Northwest China. *J. Xi'an Univ. Archit. Technol. (Nat. Sci. Ed.)* **2015**, *47*, 427–432. (In Chinese) [CrossRef]
36. Sang, G.; Han, Y.; Zhu, Y.; Liu, J. Influence of Spatial Zoning on Differentiated Indoor Temperatures in Solar Buildings. *Acta Energiae Solaris Sin.* **2016**, *37*, 2902–2908. (In Chinese) [CrossRef]
37. Dai, Y. Study on the Influence of Sunspace on Indoor Thermal Environment Comfort in Rural Dwellings in Cold Regions. Master's Thesis, Shandong Jianzhu University, Jinan, China, 2019. (In Chinese).
38. Ulpiani, G.; Giuliani, D.; Romagnoli, A.; Cataldo, M.D. Experimental Monitoring of a Sunspace Applied to a NZEB Mock-Up: Assessing and Comparing the Energy Benefits of Different Configurations. *Energy Build.* **2017**, *152*, 194–215. [CrossRef]
39. Bastien, D.; Athienitis, A.K. *Analysis of the Solar Radiation Distribution and Passive Thermal Response of an Attached Solarium/Greenhouse*; Concordia University: Montreal, QC, Canada, 2010.
40. Huang, L.; Lan, B. Analysis of Heating Energy Consumption and Indoor Thermal Environment of Traditional Dwellings in the Old City of Lhasa. *Build. Energy Effic.* **2014**, *42*, 1–7. (In Chinese)
41. Chang, Q. Research on Climate-Adaptive Design Strategies for Vernacular Buildings in the Valley Plain Area of Lhasa City. Master's Thesis, Tibet University, Lhasa, China, 2020. (In Chinese). [CrossRef]
42. *GB 55038-2025*; Residential Building Code. Ministry of Housing and Urban-Rural Development of the People's Republic of China: Beijing, China, 2025. (In Chinese)
43. Mao, Z.; Xuan, H. A Study on the Spatial Layout of Buildings Based on Thermal Buffer: Taking the New-Style Residential Houses in Lhasa as an Example. *Intell. Build. Smart City* **2025**, 88–91. (In Chinese) [CrossRef]
44. Deb, K.; Pratap, A.; Agarwal, S.; Meyarivan, T. A Fast and Elitist Multi-Objective Genetic Algorithm: NSGA-II. *IEEE Trans. Evol. Comput.* **2002**, *6*, 182–197. [CrossRef]

45. Chen, Y.; Zhang, J.; Sun, W. Co-Optimization of Passive Building and Active Solar Heating Systems Based on the Objective of Minimum Carbon Emissions. *Energy* **2023**, *275*, 127401. [CrossRef]
46. Han, X.; Fang, T.; Wang, Y.; Wang, Z.; Xu, J. Multi-Objective Optimization of Passive Design Parameters for Rural Residences Based on GA-BP-NSGA-II: A Case Study of Cold Regions in China. *J. Build. Eng.* **2025**, *112*, 113624. [CrossRef]
47. Chen, J.; Wu, Y. *Research on Design Guidelines for Solar Radiation Utilization in Urban Residential Buildings: A Case Study of Five Cities in Solar-Rich Regions*; China Architecture & Building Press: Beijing, China, 2022. (In Chinese)

Disclaimer/Publisher's Note: The statements, opinions and data contained in all publications are solely those of the individual author(s) and contributor(s) and not of MDPI and/or the editor(s). MDPI and/or the editor(s) disclaim responsibility for any injury to people or property resulting from any ideas, methods, instructions or products referred to in the content.